DEVELOPMENT OF MICROFLUIDIC DEVICES FOR INVESTIGATING SMALL MOLECULE INDUCED CHEMOTAXIS OF DENDRITIC CELLS

A Thesis Submitted to
the Graduate School of Engineering and Sciences of
Izmir Institute of Technology
in Partial Fulfillment of the Requirements for the Degree of

MASTER OF SCIENCE

in Biotechnology and Bioengineering

by
Muhammad Maaz KHURRAM

December 2023
IZMIR

We approve the thesis of **Muhammad Maaz KHURRAM**

Examining Committee Members:

_____
Prof. Dr. Erdal BEDIR
Department of Bioengineering, Izmir Institute of Technology

_____
Prof. Dr. Özlem YEŞIL ÇELIKTAŞ
Department of Bioengineering, Ege University

_____
Asst. Prof. Dr. Serkan DIKICI
Department of Bioengineering, Izmir Institute of Technology

05 December 2023

_____
Prof. Dr. Erdal BEDIR
Supervisor, Department of Bioengineering
Izmir Institute of Technology

_____
Doç. Dr. Hüseyin Cumhur TEKIN
Co-advisor, Department of Bioengineering
Izmir Institute of Technology

_____
Doç. Dr. Ali Oğuz BÜYÜKKILECI
Head of the Department of Biotechnology
Izmir Institute of Technology

_____
Prof. Dr. Mehtap EANES
Dean of the Graduate School of Education
Izmir Institute of Technology

ACKNOWLEDGMENTS

I want to extend my deepest gratitude to all the people who have made me strive ahead in this scientific career I wish to pursue. Firstly, I would like to express my gratitude to my family, who have always supported me to become what I am today.

I would like to thank my supervisor, Dr. Erdal Bedir, for allowing me to work on an interdisciplinary research project for my MS thesis. I would also like to thank my thesis jury members, Dr. Bedir, Dr. Yeşil Çeliktaş, and Dr. Dikici, for their guidance on this accomplished work. I would also like to thank my co-advisor, Dr. Tekin, for allowing me to use their lab equipment for the studies of this thesis.

Exclusively, I would like to deeply appreciate the presence of two individuals, Fatih Özefe and Nilgün Yakuboğulları. I want to acknowledge them for their perpetual teaching, guidance, and fun times throughout this journey. They always believed I could circumvent my falls and get back up even stronger in this path I wish to pursue. Thank you! A special thank you to Nilgün Yakuboğulları for invaluable Flow Cytometry experiences with her knowledge. Thank you to Fatih Özefe for the constant guidance in the Microfluidics Arena and Fabrication and for making me a Laser Master!

I want to thank Göktürk Cinel, the core support system for the last 1.5 years of this time. Your friendship and support has been irreplaceable. I want to thank the members of the Bedir Lab for their help during this time.

Also, I would like to recognize Dr. Çizmecioğlu from the Department of Molecular Biology and Genetics at Bilkent University for guiding me and embedding the persistence characteristic into my personality, striving ahead towards success.

I want to thank my friends for their unconditional support and friendship throughout my time in Turkey and for making this period of my life unforgettable.

ABSTRACT

DEVELOPMENT OF MICROFLUIDIC DEVICES FOR INVESTIGATING SMALL MOLECULE INDUCED CHEMOTAXIS OF DENDRITIC CELLS

Microfluidics is the core branch of science and technology in which interdisciplinary research is conducted with a low amount of samples in microchannels ranging from 10-100 μm. The main objective of this thesis is to design and fabricate a chemotaxis microfluidic device (CMD) from the poly-methyl methacrylate (PMMA) substrate to analyze the immune cell behavior against cancer cells. The patterns of the three-layered CMD were generated using laser ablation. During the fabrication, Power (P) and Speed (S) values were varied to determine the optimal P-S combination. Then, the structural properties of microfluidic channels in the CMD were examined via microscope. The mechanical properties and liquid handling abilities of CMDs were also investigated through tensile and leakage tests, respectively. Moreover, cell viability of DC2.4 dendritic cells (DCs) and B16-F10 murine melanoma (B16-F10) cells in CMDs sterilized through either autoclaving or UV treatment were determined to test the suitability of CMDs via Live/Dead Assay. The highest cell viability for DCs and B16-F10 was obtained in autoclaved CMDs. For the maturation of DCs before seeding into CMD, DCs were stimulated with lipopolysaccharide (LPS) and Astragaloside VII (AST-VII) at various concentrations. While the cytotoxicity of LPS and AST-VII were determined by the 3-(4,5-dimethylthiazol-2-yl)-2,5-diphenyl-2H-tetrazolium bromide (MTT) assay, the expression levels of specific chemokine receptors were also analyzed through flow cytometry. Lastly, stimulated DCs and B16-F10 were simultaneously cultured in the CMD, and the migratory behavior of DCs against B16-F10 was time-dependently studied. Consequently, CMD that provided cost-effective and rapid analysis of intercellular interactions was successfully developed.

ÖZET

DENDRİTİK HÜCRELERİN KÜÇÜK MOLEKÜL KAYNAKLI KEMOTAKSİSİNİ İNCELEMEK İÇİN MİKROAKIŞKAN CİHAZLARIN GELİŞTİRİLMESİ

Mikroakışkanlar, 10-100 μm aralığında genişliğe sahip mikrokanallarda, düşük miktarda örneklerle yürütülen, disiplinlerarası araştırmanın yapıldığı temel bir bilim dalıdır. Bu tezin temel amacı, kanser hücrelerine karşı hücresel bağışıklık davranışlarının analiz edilebileceği bir kemotaksis mikroakışkan cihazının (KMC) tasarımı ve poli-metil metakrilat (PMMA) malzemesi kullanılarak üretimidir. Üç katmanlı KMC'nin içerdiği mikroakışkan kanalların desenleri, lazer ablasyon yöntemiyle oluşturulmuştur. Üretim sırasında, en uygun Güç (G) ve Hız (H) değerlerinin belirlenebilmesi için kanal desenleri farklı G ve H değerleri kullanılarak elde edilmiştir. Ardından, KMC'deki mikroakışkan kanalların yapısal özellikleri mikroskop aracılığıyla incelenmiştir. KMC'lerin mekanik özellikleri ve sıvı tutma kapasitesi de sırasıyla çekme ve sızdırma testleri ile belirlenmiştir. Ayrıca, KMC'lerin hücre çalışmalarına uygunluğu, KMC içerisinde kültürlenen DC2.4 dendritik (DC) ve B16F10 murin melanom (B16-F10) hücrelerinin canlılıkları incelenerek belirlenmiştir. En yüksek hücre canlılığı oranları DC ve B16F10 hücreleri için otoklavlanmış KMC'lerde elde edilmiştir. DC'lerin KMC'ye ekilmeden önce olgunlaşması için çeşitli konsantrasyonlarda lipopolisakkarit (LPS) ve Astragalosit VII (AST-VII) kullanılmıştır. LPS ve AST-VII'nin hücreler üzerindeki sitotoksisite değerleri 3-(4,5-dimetiltiazol-2-il)-2,5-difenil-2H-tetrazolyum bromür (MTT) testi ile belirlenirken, dendritik hücrelerin ürettiği spesifik kemokin reseptör seviyeleri de akış sitometrisi ile analiz edilmiştir. Son olarak, uyarılmış DC ve B16-F10 hücreleriyle eş zamanlı olarak KMC içerisinde kültüre edilmiş ve DC'lerin B16F10'a karşı zamana bağlı kemotaksisi gözlemlenmiştir. Sonuç olarak, geliştirilen KMC ile hücreler arası etkileşimlerin hızlı ve uygun maliyetle analiz edilmesi sağlanmıştır.

This MSc thesis is dedicated to my family, who have always been on my side with compassion and love.
Thank you,

TABLE OF CONTENTS

LIST OF FIGURES

LIST OF TABLES

Table **Page**

ABBREVIATIONS

μL: Microliter

mm: Millimeter

μm: Micrometer

AST-VII: Astragaloside VII

CAD: Computer-aided design

CMD: Chemotaxis Microfluidic Device

CO_2: Carbon dioxide

COC: Cyclic olefin copolymer

cm: Centimeter

DCs: Dendritic cells

dPBS: Dulbecco's phosphate-buffered saline

FBS: Fetal bovine serum

imDCs: Immature dendritic cells

LoC: Lab-on-a-chip

LPS: Lipopolysaccharide

MHC: Major Histocompatibility Complex

mDCs: Mature dendritic cells

NF-κB: Nuclear Factor Kappa B

OoC: Organ-on-a-chip

P: Power

S: Speed

P10S10: 10 % Power and 10 mm s-1

P10S30: 10 % Power and 30 mm s-1

P10S80: 10 % Power and 100 mm s-1

P20S10: 20 % Power and 10 mm s-1

P20S20: 20 % Power and 20 mm s-1

P30S10: 30 % Power and 10 mm s-1

P30S80: 30 % Power and 80 mm s-1

P40S10: 40 % Power and 100 mm s-1

P50S10: 50 % Power and 100 mm s-1

P60S10: % Power and 100 mm s-1

P70S10: 70 % Power and 100 mm s-1

P80S20: 80 % Power and 20 mm s-1

P80S100: 80 % Power and 100 mm s-1

P90S10: 90 % Power and 100 mm s-1

P100S30: 10 % Power and 30 mm s-1

PTFE: Polytetrafluoroethylene

PI: Polyimide

PET: Poly(ethylene terephthalate)

PMMA: Poly-methyl methacrylate

PDMS: Poly(dimethylsiloxane)

PC: Polycarbonate

PBS: Phosphate-buffered saline

PS: Polystyrene

TLR: Toll-like receptor

CHAPTER 1

INTRODUCTION

1.1. Microfluidics

1.1.1. History and Development

Microfluidics is the core branch of science and technology that allows manipulating low amounts of fluids (10^{-9} to 10^{-18}) in microchannels ranging from 10-100 μm[1,2]. It is an interdisciplinary field where various research, such as molecular analysis, biodefence, molecular biology, and microelectronics, is performed[2]. Over the past two decades, microfluidics has rapidly developed into a state-of-the-art technology due to its small-scale size, consumption of low reagent volumes, high sensitivity, and cost-effectiveness[3].

The origins of microfluidics can be traced back to the early 1950s when the first ink-jet printing technology was established[4]. Since then, microfluidics has undergone significant developments and has been used in various applications. In the 1970s, Terry *et al.* made pioneering contributions by utilizing silicon and photolithography techniques to downscale a gas chromatograph from a laboratory-scale instrument to a miniature device. Sample vapors ranging from nitrogen, pentane, and hexane were successfully achieved using microfluidic devices produced through photolithography and chemical etching methods[5]. This micro-machined device marked a significant milestone and became one of the first lab-on-a-chip devices utilizing microfluidic technologies. Between the 1980s and 1990s, valves and pumps were introduced into microfluidic devices, thanks to the continuous advancements in microfabrication technologies[6]. For instance, Ohnstein *et al.* (1990) fabricated a one-piece silicon valve to control gas flows[7]. Researchers aimed to simultaneously integrate valves and pumps into single microfluidic devices during this period, leading to further developments. In 1988, Van Lintel and

colleagues introduced a fail-safe peristaltic pump model that prevented backflows during operations[8]. Moreover, the significant progress in these functional components had led to the birth of total analysis systems (TAS)[9]. The renaissance of microfluidics began in the 1990s with Manz *et al.*, who pioneered the development of miniaturized total chemical analysis systems (μTAS) by fabricating silicon-based devices for chemical sensing studies[10]. On the other hand, microfluidic technology was also adopted for biodefence by the Defense Advanced Projects Research Agency (DARPA) to detect chemical and biological weapons[6]. Subsequently, researchers made efforts to advance microfluidic technologies, focusing on microfabrication techniques, separation models, and devices for biological applications over the following years[11].

Towards the end of the 20th century, microfluidic technology experienced a significant breakthrough as it became increasingly involved in cell biology and biochemistry applications[12]. In 1998, Whitesides and his team used poly(dimethylsiloxane) (PDMS), an elastomeric material, to design and fabricate microfluidic systems for studying capillary electrophoresis mechanisms. Their groundbreaking work successfully demonstrated the separation of amino acids, protein-charged ladders, and DNA fragments[13]. Employing the use of a silicon-based polymer (PDMS) marked a significant milestone in microfluidics due to its excellent properties, such as biocompatibility, mechanical properties, and simplicity in fabrication techniques. In 2004, Viravaidya *et al.* employed microfluidic devices in cell-based biotechnological studies where the effects of new drugs were investigated. They fabricated a microchip containing four compartments and then cultured liver and lung cells to study the effects of drugs on cells in terms of absorption, distribution, metabolism, elimination, and toxicity[14]. Moreover, Martinez *et al.* introduced the concept of paper-based microfluidics as paper-based analytical devices in 2007. They developed a cost-effective and portable microfluidic device by patterning hydrophilic chromatography paper onto a hydrophobic polymer to study detections of glucose and proteins in urine samples. This assay, which Whitesides and his colleagues developed, paved the way for inexpensive materials to fabricate groundbreaking microfluidic devices[15].

Furthermore, microfluidic technology has undergone significant advancements, offering a wide range of functionalities in various applications, particularly in the field of biology, including point of care diagnostics (POC), nucleic acid analysis, drug discovery and development, biosensors, cell-based assays, environmental analysis, omics studies and separation studies[16]. In 2009, Liu *et al.* fabricated a polymer-based microchip to

conduct high-performance liquid chromatography of peptides and proteins using external pumps and valves[17]. Moreover, Cao et al. have also employed microfluidics to achieve highly sensitive detections of influenza virus RNA. They utilized a single-use microfluidic device that enabled robust high-throughput analysis[18].

On the other hand, microfluidics has also been integrated into cell-based analysis studies[19], offering various methods for cell culture, cell sorting, cell lysis, and cell separation. In 2010, Huh *et al.* performed revolutionary works where the lung organ was mimicked within a microfluidic device. This lung-on-a-chip model has opened new avenues for microfluidics in cell culture studies[20]. Furthermore, microfluidic technologies have been explored as tumor-on-a-chip in cancer/tumor models. For instance, Jeong et al. developed a 3D co-culture model of human colorectal tumor, where tumor spheroids were grown with fibroblasts in a microchannel to emulate an *in vivo* tumor microenvironment[21].

Consequently, the field of microfluidic technology has indeed undergone remarkable progress from its early days to its current stage. With its numerous advantages, microfluidics continues to evolve and provide a powerful platform for biotechnological and biomedical research.

1.1.2. Substrates in Microfluidics

One of the immense factors in microfluidics is selecting an optimal material for its fabrication and applications. The choice of materials can directly affect many factors, including fabrication costs, biocompatibility, and absorptivity of microfluidic devices[22]. Therefore, it is crucial to choose a suitable material for either the fabrication of microfluidic devices or its application[23].

Microfluidic devices have been fabricated using various substrate materials, including silicon, glass, paper, hydrogels, elastomers, thermoplastics, and 3D printing materials[24]. Silicon and glass were the pioneering substrates used to fabricate microfluidic devices. Silicon having semiconducting properties and has been a dominant material in microfluidic device fabrication for several decades[22]. The silanol group (-Si-OH) on its surface allows for surface modification, making it a preferred material over the developmental history of microfluidic systems. However, the high elastic modulus of

silicon limits its usage in microfluidic devices that require valves[25] and pumps[26]. Additionally, the opaque nature and low gas permeability of silicon limits their usage in long-term cell-based biological applications[25]. Glass is also a preferred material in the fabrication of microfluidic devices as it offers many advantages, such as optical transparency, low fluorescence background, surface stability, and chemical resistance[27]. It has been used in various applications involving microchannels, flow reactors, and capillaries for chromatography studies[25]. However, there are some limitations in the utilization of glass, such as the high cost of the fabrication process and the low gas permeability of glass[28,29].

As mentioned previously, using polymeric materials significantly contributes to developing microfluidic devices. Especially one of the elastomeric polymers, PDMS, has played an essential role in the fabrication of polymeric microfluidic devices. PDMS was first introduced by Duffy *et al.*[13] due to its numerous advantages, such as optical transparency[30], easy-to-operate, and biocompatibility[31]. However, it is important to note that PDMS is a hydrophobic polymer composed of repeating units of -OSi(CH3)2, where the presence of CH3 units on its surface makes it inherently hydrophobic[32]. To overcome this limitation, surface treatments such as oxygen plasma treatment can be employed to convert the hydrophobic methyl groups to hydrophilic silanol groups (Si-OH)[32]. In addition to elastomeric polymers, thermoplastics are also used in the fabrication of microfluidic devices, such as polycarbonate (PC), polystyrene (PS), cyclic olefin copolymer (COC), poly (methyl methacrylate) (PMMA). As these polymers are sustainable and renewable, they also provide cost-effective fabrication of microfluidic devices[33,34]. Moreover, thermoplastics are optically transparent[35], biocompatible, and gas permeable materials[36]. Compared to PDMS, thermoplastic-based microfluidic devices offer advantages and overcome some limitations, such as solvent swelling, molecule absorption, and low rigidity[36]. Recently, PMMA has become the primary polymer material used for several microfluidic applications. In one of the studies, Persson *et al*. fabricated the microfluidic device from PMMA material to culture human endothelial cells in the long term. Fabrication of 36 devices was performed in five hours using the laser ablation technique. In the fabricated device, migration of THP-1 monocytes towards endothelium cells was examined[37]. Moreover, quite recently, a PMMA-based 3D fluidic channel platform was developed by Mortelmans *et al.* to detect SARS-CoV-2 antibodies, such as IgG and IgM, serologically[38].

Paper and hydrogels have also been adopted as substrates in some microfluidic studies. As the paper is biocompatible, it also provides cost-effective, easy, and rapid fabrication of microfluidic devices[15,39]. Pupinyo *et al.* used paper materials to fabricate a paper-based microfluidic device where B16F10 melanoma cells were cultured in a three-dimensional (3D) environment[40]. In a recent study, Ozefe *et al*. fabricated a µPISA device via the laser ablation technique to rapidly diagnose Hepatitis C Virus (HCV) from blood samples[41]. Moreover, hydrogels are also used to fabricate microfluidic devices due to their biocompatible properties[24] and low cost[29].

Table 1.1. Common substrates used for the fabrication of microfluidic devices.

Substrate	Advantages	Limitations	Application	References
Silicon	Good mechanical properties Ease of sterility Biocompatible Low absorption	High fabrication costs Difficult fabrication High Young's modulus Low oxygen permeability Low optical clarity	Separation of gas vapors Valve development modulating gas flows Chemical sensing	5,7,10,17,25–27
Glass	Good mechanical properties Ease of sterility Optically transparent Low absorption	High fabrication costs Difficult fabrication High Young's modulus Low oxygen permeability	Capillary electrophoresis On-chip high temperature reactions Solvent extraction	22,24,29
Paper	Ease of fabrication Low fabrication costs Ease of sterility Chemical and biological modifications Biocompatible Ease of fluid flow (capillary action)	Poor mechanical strength Hydrodynamic resistance Challenging sterilization Low optical clarity	Rapid diagnostic testing Paper-based scaffold cell culture Environmental monitoring	15,25,40–42
Hydrogels	Low fabrication costs Ease of fabrication Low Young's modulus High oxygen permeability Biocompatibility Chemically modifiable Optically transparent	Demanding sterilization	Sensors Tissue engineering 2D and 3D scaffold-based culture	22,23,29,43
Elastomers (PDMS)	Low cost of fabrication Ease of fabrication Optically transparent High oxygen permeability Highly elastic Biocompatibility	Chemical resistance Absorption of biomolecules Water evaporation from channels	Capillary electrophoresis Analytical chemistry Lab-on-a-chip devices	30,31,34,44–48
Thermoplastics (PC, PS, COC, PMMA)	Low fabrication costs Good mechanical properties Ease of sterilization Biocompatible Chemical modifications Optically transparent Low absorption Rapid prototyping	Variable oxygen permeability	Tissue culture Immunoassays Protein and DNA analysis	33–36,46,47,49,50

1.1.3. Fabrication Techniques

Microfluidic devices are produced through various fabrication techniques, including chemical and mechanical processing, laser ablation, and 3D printing[51]. The choice of fabrication technique mainly depends on the material used, which means that different substrates require different fabrication methods. Two main techniques are used in the fabrication of microfluidic devices, such as photolithography and soft lithography techniques.

Photolithography, also known as optical lithography, involves transferring geometric shapes from an optical mask onto the surface of a silicon wafer using ultraviolet (UV) light[52]. The process of photolithography includes substrate cleaning, application and implementation of the photoresist, exposure to UV light, baking, etching, and the removal of photoresists[53]. This technique is renowned for fabricating devices with high-resolution features, typically around 5 μm[53]. Although photolithography offers high resolution, it requires sophisticated equipment and clean room facilities, which increases the cost of operation[54].

As an alternative method, Duffy *et al*. introduced soft lithography techniques to fabricate microfluidic devices[13]. Soft lithography, also commonly known as the stamping technique, is a non-photolithographic technique implying self-assembly and replica molding based strategies for the fabrication of microfluidic devices[55]. In soft lithography, elastomeric stamps, molds, or masks are used instead of rigid photomasks to create micro-patterns and structures for microfluidic devices. Compared to conventional photolithography, soft lithography provides several advantages, such as cost-effective and easy fabrication costs[56]. Soft lithography can be classified into several fabrication methods, such as micro-contact printing (μCP), replica molding, cast molding, solvent-assisted molding, hot embossing and injection molding, 3D printing, and laser ablation[56].

Hot embossing is a technique that involves heating polymer plates above the glass transition temperature, applying pressure to press a master mold into a polymer substrate, followed by cooling and detachment of formed microstructures[57]. As an advantage, hot embossing offers less residual stress on thermoplastic surfaces and provides high replication accuracy, which supports the mass production of microfluidic devices[58].

However, it requires an expensive master mold and has difficulties in forming channels or microstructures with a high aspect ratio[59].

Injection molding is another technique used in the fabrication of thermoplastic microfluidic devices[60]. In this process, thermoplastic polymer substrate is melted and then injected into cavities of molds already prepared. The molten polymer is next cooled below the glass transition temperature, resulting in the formation of micro-sized patterns. The molding process is conducted under constant pressure to compensate for the shrinking of polymer substrate during solidification while the temperature is gradually decreased. The entire process typically takes a few minutes[61]. Compared to other techniques, injection molding offers a superior surface finish; however, the cost of operation is high. Moreover, it is hard to operate fabrication with injection molding for polymers having high polarity[62]. On the other hand, assembling individual layers is also difficult[63].

Another technique that facilitates the fabrication of microfluidic devices or biosensors is 3D printing. This technology, also known as smart additive manufacturing[64], has been developed over the last decade to produce microfluidic devices[65]. 3D printing enables layer-by-layer and rapid fabrication of microfluidic devices. For this technique, bio-inks are commonly used[66]. The fabrication process begins with the design of a 3D computer-aided design (CAD) model, and then a 3D printer is used to fabricate this designed model. Even if 3D printing offers a cost-effective and rapid fabrication, it has certain limitations, such as lower resolution and poor surface quality[67].

Lastly, laser micro-machining is another rapid fabrication technique where a laser beam is focused onto the surface of the substrate to remove material. Commonly used substrates for the laser micro-machining includes polytetrafluoroethylene (PTFE), polyimide (PI), poly(ethylene terephthalate) (PET), and poly(methyl methacrylate) (PMMA)[68]. In this technique, ablation occurs on the surface of substrate when the material absorbs enough energy from the laser beam to be either melted or vaporized[68]. As a laser source, UV excimer laser[69] and CO_2 laser[70] have been used. Klank *et al*. used CO_2 lasers for the first-time to fabricate microfluidic device from PMMA substrate in 2002[70]. This technique offers rapid production of microfluidic devices[71,72]. In literature, various CO_2 lasers are available to be used in the fabrication process. These lasers offer three different strategies that are focused processing, defocused processing and raster scanning method[71]. In raster mode, Gaussian-shaped microchannels are produced by laser treatment leaving an engraved region onto the substrate[73,74].

Table 1.2. Fabrication techniques employed in microfluidic devices.

Fabrication Technique	Advantages	Drawbacks	References
Photolithography	High resolution Suitable for many substrates	Complex fabrication High cost Requires clean-room facilities Longer fabrication times	5,7,51,54,56
Soft Lithography	Low fabrication costs Ease-to-operate Suitable for many substrates	Low resolution Easy to deform	13,14,56,57
Hot Embossing	High replication accuracy Moderate fabrication cost Mass production	Expensive master molds Low resolution Possible breakage	57,58,75–77
Injection Molding	Superior finish High reproducibility	High cost	50,60–62,78,79
3D Printing	Low cost Rapid fabrication	Poor surface quality Low resolution Compatibility issues	72, 74, 75
Laser Ablation	Low cost Ease-to-operate Rapid fabrication	Surface roughness	69,71,72,80,81

1.2. Immune System and Dendritic Cells

The immune system is crucial in defending the body against foreign pathogens and infections[82]. It consists of a variety of cells, molecules and many defined organs that work together and provides the protection of the body against foreign pathogens and infections through immune responses[82,83]. There are three major levels of defense including the skin (the primary physical barrier)[84], innate immune responses and adaptive (acquired) immune responses[85].

Innate and adaptive immune responses are activated when the physical barrier, the skin, is breached. The innate immune response, also known as the first line response, provides an immediate host defense against foreign invaders. In innate response, the phagocytic cells, including macrophages, monocytes, and neutrophils, recognize foreign threats and release inflammatory mediators for body protection[86]. Whereas, adaptive immune responses, also known as second line response, provide antigen-dependent and antigen-specific responses by T and B lymphocytes. In this response, antigen-presenting cells, such as dendritic cells (DCs), present specific antigens to lymphocytes, enabling T cell homing[87].

DCs are antigen-presenting immune cells that are derived from the hematopoietic bone marrow progenitor cells. DCs link innate and adaptive immunity by initiating and modulating adaptive immune responses through presenting processed peptides derived from the lymphoid and peripheral tissues[88–92]. Therefore, DCs play a crucial role in the adaptive arm of the immune system in addition to their role in innate immune responses. These cells are normally found in an immature state where they express low levels of co-stimulatory molecules (CD80, CD86, CD83 and MHC II) and secrete low amounts of cytokines (IL-12, IL-10 and TNF)[93,94]. However, DCs undergo a systematic process of maturation and activation by various stimuli, including pathogens, double-stranded (ds) viral DNA[95](Soto), lipopolysaccharide (LPS)[96], pathogen-associated molecular patterns (PAMPs)[97], and CpG oligodeoxynucleotides (CpG-ODNs)[98]. Conversely, mature dendritic cells (mDCs) express high levels of co-stimulatory molecules and secrete cytokines for the functional polarization of T cells[99]. Maturation of DCs allows for the subsequent activation of naïve T and B cells into antigen-specific T cells and antibody-releasing plasma cells, respectively[100,101]. Also, mDCs have upregulated expressions of chemokine receptors on their surface, for example the upregulation of CCR7 promotes chemotaxis of DCs through the CCL21/CCR7 axis[102,103].

Chemotaxis refers to the directional movement of cells guided by an extracellular gradient[104]. These migratory abilities of DCs are crucial for their coordinated functions in inflammation and immune responses, thereby linking adaptive and innate immunity. The migration of DCs is achieved under various immunological conditions such as the presence of chemokines[105].

Chemokines are small proteins secreted by various cell types that play a crucial role directing immune cell trafficking and mediating lymphoid tissue developments[106]. They are classified into four families based on the position of a conserved cysteine motif, which includes CC, CXC, XC and CX3C[107]. The migration of mDCs is regulated by these small chemokines. For example, chemokine (C-C motif) ligand 19 (CCL19) and 21 (CCL21) direct migration of DCs into the lymph nodes by the expression of affiliated C-C chemokine receptor type 7 (CCR7) receptor expressed on mDCs[108]. Consequently, chemotaxis of mDCs occurs due to higher expression of CCR receptors on the cell surface corresponding to cognate chemokines through an increasing chemokine gradient to initiate specific immune responses[109].

Table 1.3. Murine chemokine receptors and their conjugate chemokine ligands associated with dendritic cell migration.

Chemokine Receptor	Chemokine Ligands	References
CCR1	CCL3, CCL9, CCL5, CCL15	110–112
CCR2	CCL2	110,113–115
CCR5	CCL2, CCL3, CCL4, CCL5	110,116–118
CCR6	CCL20	110,119
CCR7	CCL19, CCL21	110,120,121
CCR9	CCL25	110,122

1.3. Immune System Applications through Microfluidics

Immunological approaches have been historically carried out using 2D *in vitro* cell cultures[123] and *in vivo* animal models[124]. 2D *in vitro* models could not successfully emulate *in vivo* physiological microenvironments, and rodent animal models have shown significant differences in immune system characteristics compared to humans[125,126]. To overcome these limitations in each model, sophisticated micro-engineered technologies have been developed to study the diverse behavior of immune cells and their interactions with other cells[127]. Until today, microfluidic devices have been used in single-cell and tissue level studies for the characterization of immune cells and understanding cell-cell interactions, respectively. These developments have mainly focused on the characterization of individual immune cells through the investigation of their signaling pathways, action dynamics, secretion, and cellular communication in the presence of external and/or internal stimuli. Also, 3D microfluidic devices have been developed to investigate cell-cell interactions, such as immune-tumor cell interaction in tumor-on-chip platforms.

Over the last decade, microfluidic technology has been integrated into the applications of single-cell immune analysis due to its numerous advantages such as high throughput and real-time analysis processing with small amounts of reagent volumes[127]. Single-cell analysis using microfluidics has established for the understanding of immune cell isolation and quantification, quantification of signaling molecules, signaling pathways associated with immune responses and understanding immune cell motility in

response to foreign pathogens or tumors. In a pioneer study by Cheng *et al.*[128], a microfluidic device was developed to count label-free CD4+ T cells from HIV positive blood samples of patients, whole blood samples were quantified to obtain cell capture specificity using cell affinity chromatography to distinguish blood samples from HIV positive or negative patients. Also, immune cells separations have been conducted utilizing microfluidics, a single microfluidic channel device was developed by Li *et al.*[129] to separate B and T lymphocytes from a cell mixture using specialized antibodies specific for B and T cells. Moreover, Qiu *et al.*[130] developed a cell membrane-anchored fluorescent aptamer sensor in combination with a droplet microfluidic platform to detect IFN-γ cytokine secretion at a single-cell level from T cells. The regulation of immune cells controls with several key players of the innate pathways including the cGAS-STING pathway[131], Toll-like receptor pathway (TLR)[132], and NF-κB signaling pathway[133]. Microfluidic technologies have been employed by Campisi *et al.*[134] to evaluate tumor-vasculature interactions where tumors sense dsDNA through the cGAS-STING pathway for innate immune signaling. Also, Tay *et al.*[135] fabricated a high-resolution microfluidic device to analyze the activation of TLR-4 pathway measuring the NF-κB activity in macrophages in terms of its translocation kinetics at an individual cell level.

The motility of immune cells is one of the key aspects of their function, enabling them to detect and respond to foreign invaders. While these highly motile cells continuously circulate through the blood and lymphatic systems, they quickly exit circulation and migrate to the site of infection, where the foreign invader is found to initiate immune responses[136,137]. Microfluidics has been integrated to study the motility of immune cells, where Businaro *et al.*[138] established a co-culture platform to observe the motility of spleen cells towards B16-F10 cells.

Neutrophils and DCs are the premier immune cells to arrive at the inflammation site, helping maintain homeostasis[139]. Chemokines are essential in regulating immune cell migration by coordinating immune cells at the inflammation sites[140]. Microfluidics has offered unique opportunities to study immune cell migration in real-time, under varying chemokine gradients and various tumor-induced factors [141,142]. In pioneering works, Jeon *et al.*[143]developed a microfluidic gradient generator platform to establish stable and soluble IL-8 gradients to observe neutrophil migration. Lin *et al.*[144] used a similar gradient generator microfluidic device to study neutrophil chemotaxis with increasing IL-8 gradients, showing that neutrophil migration was influenced by an IL-8 concentration. More recently, Ren *et al.*[145] developed a skin-on-a-chip (SoC) model to study the

transmigration of human-derived T cells in an increasing CCL20 chemokine gradient and in response to TNF-α induced skin inflammation.

Microfluidics has also been integrated into studying the chemotaxis of mDCs towards an increasing chemokine gradient and by tumor-induced factors. Real-time analysis of DC migration using microfluidics has allowed extended observation periods with the aid of image processing techniques[146]. One of the earliest works for DC chemotaxis was performed by Haessler *et al.*[120] and Ricart *et al.*[121], who used a three-channel device and a chemokine gradient generator, respectively, to demonstrate the chemotaxis of mDCs stimulated with LPS and TNF-α in response to a gradient of the CCL19. Moreover, co-culture studies using microfluidics have also been established by Businaro *et al.*[138], where motility of collective spleen cells towards B16 melanoma cells was observed. In this study, immune cell migration was monitored using fluorescence microscopy and time-lapse recordings, providing valuable insights into immune-cancer cell interaction and immune cell behavior in tumor microenvironment. Furthermore, Hwang *et al.*[147] investigated mDC chemotaxis in response to tumor-induced factors, using a 3D PDMS-based microfluidic device. In this study, the migration of mDCs towards a CCL19 chemokine gradient and breast cancer cells in the collagen matrix was individually examined under static conditions. On the other hand, Aizel *et al.*[148] developed a microfluidic device to visualize the single DCs going through chemotaxis over a longer period[148]. Another interesting microfluidic platform to study the chemotaxis of human mDCs towards colorectal cancer (CRC) cells was developed by Parlato *et al.*[149]. DCs were matured by IFN-α, and CRC cells were treated with Romidepsin (RI) to produce the CXCL12 chemokine under static conditions. Lastly, Atalis *et al.*,[150] modulated DC chemotaxis by soluble and biomaterial-loaded toll-like receptor agonists within a microfluidic device. The authors reported that the chemotaxis of DCs was observed in an increasing CCL19 and CCL21 gradient. This study also showed the effects of adjuvant type and its delivery method on the DCs migration.

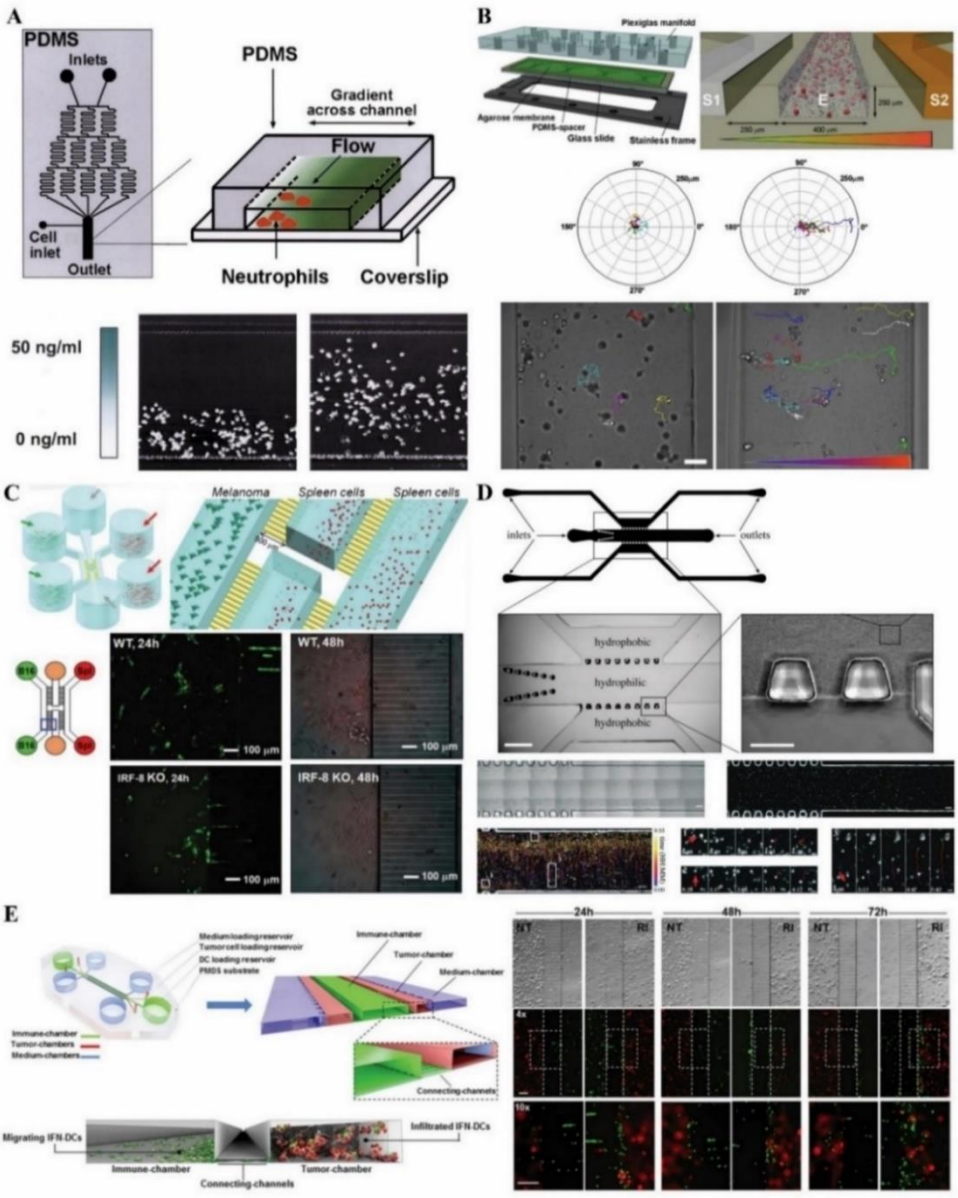

Figure 1.1. Microfluidic devices for studying immune cell migration. (A) The chemotaxis of neutrophils in a linear gradient of IL-8 from 0 to 50 ng/mL[143], (B) A 3D microfluidic chemotaxis device containing an agarose-filled central channel for studying mDC chemotaxis in an increasing chemokine gradient[120], (C) A co-culture microfluidic device for spleen cell migration, Green: B16 cells and Red: Spleen cells[138], (D) A chemotaxis microfluidic device consisting of hydrophobic and hydrophilic regions for a longer period of chemotaxis analysis of mDCs in an increasing CCL19 gradient[148], (E) A 3D microfluidic device examining mDC chemotaxis through centrally located microchannels towards RI treated CRC cells[149].

1.4. Aims of Thesis

Developing novel microfluidic devices for cell culture applications has demonstrated the importance of mimicking 3D in vivo microenvironments fabricated in small, portable, and cost-effective microdevices. Studies have shown that the interactions of immune cells with cancer cells provide insight into immunotherapy options against cancer cells.

The main objective of this thesis is to develop a three-layered, cost-effective chemotaxis microfluidic device (CMD) using only Poly(methyl methacrylate) (PMMA) as the fabrication substrate using 1-mm thick PMMA layers for the top, middle, and bottom layers. For this purpose, the laser ablation methodology is utilized to develop an adequate platform for the culture of DCs and B16-F10 cells.

The second aim of this thesis is to observe the chemotaxis of mDCs towards B16-F10 in the developed CMD along the CCR5/CCL2-CCL5 axis. For this purpose, we aim to analyze the CCR5 expression levels on imDCs and mDCs and the CCL2 and CCL5 chemokine expression levels in B16-F10 by flow cytometry to observe the directional migration of LPS-AST-VII stimulated mDCs towards CCL2/CCL5 chemokines expressed by B16-F10 cells.

CHAPTER 2

MATERIALS AND METHODS

2.1. Materials

2.1.1. Consumable Materials

Poly (methyl methacrylate) (PMMA) sheets (Depodanmalzeme), double-sided adhesive tape (3M, GPT-020), ethanol (Honeywell, 24194), and 2-propanol (IPA) (Isolab, 961.023) were purchased for the fabrication and optimization of CMDs. Blue ink was used for CMD leakage testing.

DC2.4 dendritic cells (Sigma-Aldrich, SCC142), B16-F10 melanoma cells (ATCC, CRL-6475), RPMI 1640 medium (Gibco, 52400025), Fetal Bovine Serum (FBS) (Gibco, 10270106), Penicillin/Streptomycin (Gibco, 15140122), 2-Mercaptoethanol (Merck, M6250), MEM Nonessential Amino Acids (NEAA-B) (Capricorn Scientific, NEAA-B), Trypsin-EDTA (Gibco, 25200056), Dulbecco's Phosphate Buffer Saline (dPBS) (Gibco, 14190144), MTT assay kit (Sigma Aldrich, CT01), Live/Dead Cell Viability Kit (AAT Bioquest, 22789), Bovine serum albumin (BSA) (AFG Bioscience, 221137), Sodium Azide (Sigma Aldrich, 71290), Anti-mouse CD16/32 Antibody (Biolegend, 101302), Anti-mouse CCR5 (CD195) (Biolegend, 107017), Intracellular Staining Permeabilization Wash Buffer (10X) (Biolegend, 421002), APC anti-mouse/rat/human MCP-1 antibody (Biolegend, 505909), PE anti-mouse CCL5 (RANTES) antibody (Biolegend, 149103) and Fixation Buffer (Biolegend, 420801) were purchased for flow cytometry studies.

Lipopolysaccharide (LPS) (Sigma Aldrich, L2630) was purchased to stimulate dendritic cells. Astragaloside VII (AST-VII) was donated by Bionorm Natural Products, Izmir, Turkey. CytoTrack™ Green (AB138891, Abcam) and CytoTrack™ Red (AB138893, Abcam) were purchased for chemotaxis assays.

2.1.2. Computer Programs and Instruments

AutoCAD 2023 (Autodesk), ZEN Lite (Zeiss), GraphPad Prism (San Diego, CA) Laserbox 40W (Makeblock), Axio Observer Microscope (ZEISS), Axio Vert.A1 (ZEISS), Mechanical Testing Machine (Shimadzu AG-I 250kN), Laminar air flow cabinet (Nuve, LN 090), Multiskan™ GO Microplate Spectrophotometer, (Thermofisher, N10588), FACSCanto (BD), were utilized for the fabrication, characterization of CMDs and visualization of DC2.4 chemotaxis towards B16-F10 cells.

2.2. Methods

The design and fabrication of the Chemotaxis Microfluidic Device (CMD) were conducted in several stages. Firstly, the CMD was designed with computer-aided AutoCAD 2023, and then the laser ablation technique was operated to pattern desired shapes onto the PMMA sheets. For precise patterning, laser operating modes (vector and raster) were validated for various Power (P) and Speed (S) values, and the optimal fabrication parameters were determined. Subsequently, each layer manufactured for the CMD was assembled through a solvent-assisted bonding technique. Moreover, the structural features of the CMD were characterized in terms of its border/channel dimensions, liquid handling capacity, and bonding strength. Then, the fabricated CMD was optimized for cell culture studies. The suitability of the CMD for DC2.4 dendritic cells (DCs) and B16-F10 melanoma cell (B16-F10) culturing was tested using live/dead assay.

On the other hand, DC2.4 cells were stimulated with LPS and AST-VII at different concentrations for their maturation. Also, the viability of treated DC2.4 cells was analyzed by MTT Assay. Molecular analysis of chemokine receptor expression on stimulated DC2.4 cells was conducted through flow cytometry analysis. Finally, CMD was utilized to observe the chemotaxis of DC2.4 cells towards B16-F10 to investigate intercellular communication between immune and cancer cells.

2.2.1. Design of Chemotaxis Microfluidic Device (CMD)

The CMDs were designed using AutoCAD 2023. It mainly consists of two main lateral channels (individually for DC2.4 and B16-F10) and centrally located microchannels to visualize immune cells' chemotaxis toward cancer cells (Figure 2.1). In the CMD, a top lateral channel was designed for DC2.4 cells with the shape of an inverted U. The vertical and horizontal components of the DC channel were 7 and 28 mm, respectively. On the other hand, a straight B16 channel was generated with a length of 33 mm at the bottom part of CMD for B16F10. The widths of each lateral channel were 1 mm. The CMD also contains inlet and outlet regions with 1 mm radii for both DC and B16 channels (Figure 2.1A).

Additionally, eleven centrally located microchannels, having a width, length, and depth of 300, 650, and 150 μm, were designed, respectively. In principle, each microchannel was designed 1000 μm away from each other (Figure 2.1B).

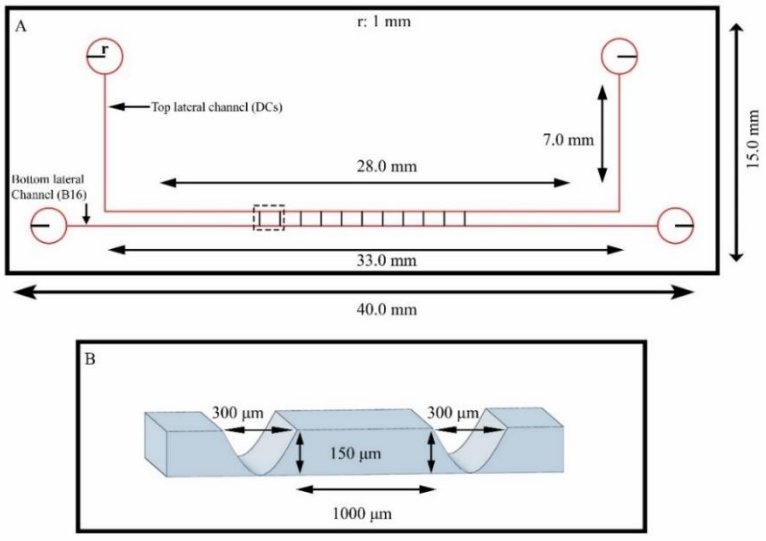

Figure 2.1. Design of the Chemotaxis Microfluidic Device (CMD). (A) Technical drawing for CMD, containing top and bottom lateral channels for DCs and B16F10, respectively, and centrally located chemotaxis microchannels. The radius of the inlets and outlets is denoted as “r” and equals 1 mm. (B) Gaussian-shaped centrally located chemotaxis microchannels.

2.2.2. Validation and Optimization of the Laser Operation Modes

CO_2 laser cutter (Makeblock, Laserbox) with a maximum power of 40W was used to conduct the laser ablation technique leading towards CMD fabrication. The laser cutter was utilized with two ablation modes, vector and raster, to ablate DC and B16-F10 lateral channels and engrave microchannels from a PMMA substrate, respectively. Numerous Power (P) and Speed (S) values were offered by the CO_2 laser, where the maximum P and S were 40 watts (corresponding to 100%) and 80 mm/s, respectively. For the optimization of vector and raster modes, eighty different combinations of P-S values were studied in this thesis (Table 2.1).

Table 2.1. Eighty different Power (P) and Speed (S) combinations employed in the fabrication process for the vector (cutting) and raster (engraving) modes.

Power (%)	**Speed (mm/s)**							
10	10	20	30	40	50	60	70	80
20	10	20	30	40	50	60	70	80
30	10	20	30	40	50	60	70	80
40	10	20	30	40	50	60	70	80
50	10	20	30	40	50	60	70	80
60	10	20	30	40	50	60	70	80
70	10	20	30	40	50	60	70	80
80	10	20	30	40	50	60	70	80
90	10	20	30	40	50	60	70	80
100	10	20	30	40	50	60	70	80

The methodologies employed to validate and optimize the vector mode for DC and B16 lateral channels are described here. Firstly, CMD drawings were exported to the Laserbox software; and then each of these eighty P-S combinations were tested to check whether they ablate the 1 mm thick PMMA or not. Subsequently, the combinations (P40S10; P50S10; P60S10; P70S10; P80S10; P80S20; P90S10; P90S20; P100S10; P100S20) that successfully cut the PMMA were subjected to determine their error rates during the vector mode operation. To define error rates for each P-S combination,

rectangles with various widths (500-1000 μm) were cut using vector mode; then the obtained with values were determined by analyzing images captured via bright-field microscope (Axio Observer, Zeiss). Sequentially, the obtained width values were compared with their theoretical values to calculate the error rates of each P-S combination through Formula 1.

$$\text{Formula 1. } Error\ Rate\ = \frac{Obtained\ Length - Drawn\ Length}{Drawn\ Length} \times 100 \quad (2.1)$$

After determining the P-S value that gave the lowest error rate, a graph showing theoretical and obtained widths was plotted to define an equation to obtain 1000 μm (Formula 2).

$$\text{Formula 2. } y = 1.0618x + 79.569 \text{ (y= Obtained width; x= Theoretical width)} \quad (2.2)$$

Additionally, the raster mode was validated to define the effects of P and S on the Gaussian-shaped centrally located microchannels. Again, the pool of eighty P-S combinations (Table 2.1) was utilized to engrave microchannels to select optimal P and S values according to the required dimensions of the CMD design. After engraving, microchannels were visualized and analyzed via a microscope.

2.2.3. Fabrication of the Chemotaxis Microfluidic Device

The fabrication of the CMD was executed by laser ablation through optimized P and S parameters for each operation mode. Validated vector and raster operation modes were used to generate lateral channels and microchannels of the CMD, respectively. After patterning the microfluidic channels on CMD's PMMA layers, each layer was assembled via two techniques (Table 2.2).

AT 1 utilized the CMD as a three-layered device, ablating the middle layer with the aid of vector and raster modes, obtaining top and bottom lateral channels and the

centrally located microchannels, respectively. A double-sided adhesive was placed on both sides of the PMMA substrate before ablating the middle layer (Figure 2.2).

Table 2.2. Assembly techniques for appropriate bonding of layers in CMDs.

Assembly Technique	Definition
Assembly Technique 1 (AT 1)	A three-layered CMD with double-sided adhesive on both sides of the middle layer, having a top layer (inlet and outlets) and a bottom support layer.
Assembly Technique 2 (AT 2)	A three-layered CMD having a top, middle, and bottom layer assembled using thermally assisted solvent bonding.

AT 2 is a thermally assisted solvent bonding technique with ethanol (EtOH) and isopropyl alcohol (IPA). For this technique, the individual layers in CMD were first ablated using the vector and raster mode, respectively. Later, solvents were implemented, spraying solvent onto the bottom layer. The middle layer was slid onto the bottom layer to remove excess solvent, and then the top layer was slid onto the middle layer to which solvent was sprayed (Figure 2.3). At that point, any remaining excess solvent was removed from the inlets and outlets. Finally, the assembled CMD devices were carefully placed into the vacuum oven. Table 2.3 shows each condition employed for assembling CMD layers.

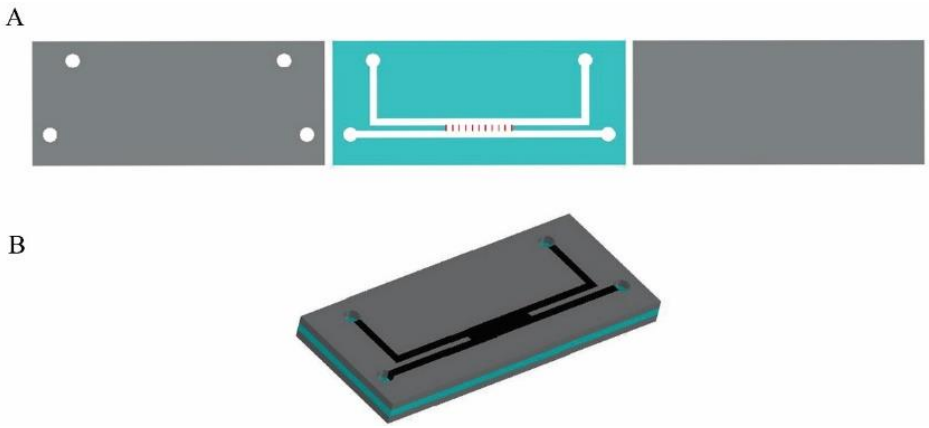

Figure 2.2. Assembly Technique 1. The double-sided adhesive was utilized on both sides of the middle layer for assembly of CMD. (A) Individual layers of CMD. (B) Three-layered CMD.

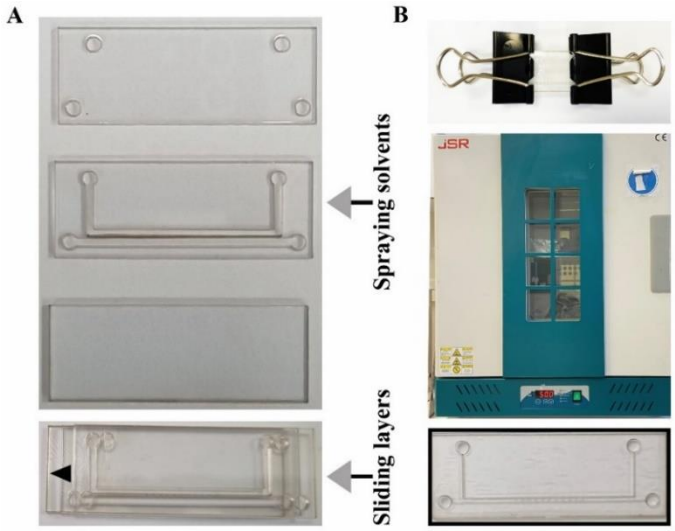

Figure 2.3. Assembly Technique 2: Thermally-assisted solvent bonding technique. (A) Individual layers of CMD. (B) Three-layered CMD.

Table 2.3. Solvent bonding conditions employed in AT 2.

Solvent Concentration	Oven Temperature	Time (min)
50 %	60°C	5
		10
		20
	70°C	5
		10
		20
60 %	60°C	5
		10
		20
	70°C	5
		10
		20
70 %	60°C	5
		10
		20
	70°C	5
		10
		20
80 %	60°C	5
		10
		20
	70°C	5
		10
		20

2.2.4. Characterization of Chemotaxis Microfluidic Device

CMDs were characterized in terms of their liquid handling capacity and mechanical strength via leakage and tensile strength tests, respectively. First, assembled CMDs using thermally assisted bonding techniques were subjected to leakage tests. For that purpose, blue ink was injected into the microchannels in CMDs assembled via either ethanol or isopropyl alcohol to test the permanent bonding of layers. Secondly, the CMDs that showed no signs of bleeding were carefully placed onto the clamps of the tensile machine. Then, they were pulled at a speed of 0.5 mm/min to determine the tensile strength of CMDs. The obtained data (Force-kN vs. stroke-mm) were used to calculate stress and strain values for determining the maximum tensile strength of CMDs through **Formula 3**.

Formula 3. $Stress = \frac{Force}{Area\ of\ Surface}$ (2.3)

Lastly, the required sample amounts for microchannels in CMDs were determined. For that purpose, varying amounts of blue ink dyes were separately injected into the top and bottom channels.

2.2.5. Cell Culture

2D *in vitro* cell culture studies were performed for thawing and culturing DCs dendritic and B16-F10 cells by following the manufacturer's instructions. DCs cells were maintained in RPMI-1640 medium with 10 % Fetal Bovine Serum, 1 % Penicillin/Streptomycin, 50 μM 2-mercaptoethanol, and 1 % non-essential amino acids. B16-F10 cells were maintained in RPMI-1640 medium with 10 % Fetal Bovine Serum, 1 % Penicillin/Streptomycin and 50 μM 2-mercaptoethanol. When the confluence was around 80%, they were trypsinized and placed into several tissue flasks to expand their number. Lastly, stock cultures for each cell line were created and kept in liquid nitrogen for further experiments.

2.2.6. Validation of CMDs for Cell Culture Studies

The suitability of three-layered CMDs for cell-based studies were examined before their use in cell culturing. To test the cell viabilities inside the CMDs, CMDs were sterilized by available sterilization techniques, including autoclaving and UV treatment. While CMDs were autoclaved with exposure to saturated steam at 121°C for 20 minutes, UV light was also exposed to each side of other CMDs for 45 minutes. After the sterilization of CMDs by autoclaving and UV treatment, the cellular viabilities of B16-F10 and DCs were determined by live/dead assay. For this purpose, B16-F10 and DCs (cell number: 10^4 cells) were individually suspended in 60 µL of cell culture media and then injected into the CMD channels. At specific time points for 48 hours, 20 µL of dye solution that contains CytoCalcein and Propidium Iodide (PI) were pipetted into the inlets. After adding dye solution into the channels, CMDs were incubated for 30 minutes at 37°C in a humidified CO_2 incubator. Lastly, the fluorescence images for each specific time point using a fluorescence microscope (Zeiss Axio Observer).

2.2.7. Flow Cytometry Analysis

DC2.4 cells were subjected to surface marker staining to assess the expression of chemokine receptor 5 (CCR5). After DC2.4 cells stimulation, the cells were detached and suspended in FACS (Fluorescence Activated Cell Sorting) buffer, which was prepared by dissolving 5 g of BSA (Bovine Serum Albumin) and 125 mg sodium azide in 500 mL 1X PBS. Mouse CD16/32 antibody was added into each well and incubated for 10 minutes on ice. Then, anti-mouse CCR5 (CD195) – PE/Cy7 was added and incubated on ice in the dark for 40 minutes. Next, the cells were washed with a FACS buffer and centrifuged 350 x g for 5 minutes. The fixation buffer (4% paraformaldehyde) was added to fix the cells on ice for 15 minutes. Finally, the cells were washed and resuspended in FACS buffer to analyze CCR5 levels in the flow cytometer (BD FACSCanto).

B16-F10 cells were analyzed for chemokine (C-C motif) ligand 2 (CCL2) and chemokine (C-C motif) ligand 5 (CCL5) expression levels up to 72 hours. Brefeldin-A

was added into B16-F10 cells 5 hours before performing intracellular staining. B16-F10 cells were detached and suspended in the FACS buffer. The cells were fixed with a fixation buffer for 20 minutes in the dark on ice. After washing with FACS buffer, the fixed cells were washed with an Intracellular Staining Permeabilization Wash Buffer (Biolegend) and centrifuged at 350 x g for 5 minutes (twice). Anti-mouse CCL2 - APC and anti-mouse CCL5 – PE dye cocktail were added into the cells and incubated for 20 minutes in the dark on ice. The cells were washed with the Intracellular Staining Permeabilization Wash Buffer and centrifuged at 350 x g for 5 minutes. Finally, the cells were resuspended in FACS buffer, and cell fluorescence was assessed using flow cytometry (BD FACSCanto). The data were analyzed with FlowJo software version 10.

2.2.8. Cytotoxicity Assessment of Small Molecules on of DC2.4 cells with LPS and AST-VII

DCs were stimulated by treatment with various amounts of small molecules (LPS and AST-VII) for their maturation. In this regard, the cytotoxicity of LPS and AST-VII on DCs were first analyzed by MTT assay. Moreover, the effects of LPS and AST-VII on the expression of chemokine receptors in DCs were determined by flow cytometry.

For cytotoxicity assessment, DCs (5-10 x 10^3 cells) were suspended in 200 µL of RPMI-1640 medium and then seeded in a 96-well plate. Later, the cells were incubated overnight. On the following day, the cells were treated with (i) 100 ng/mL concentration of LPS and (ii) 2 µM, (iii) 5 µM concentration of AST-VII; and (iv-v) also co-treated with LPS (100 ng/mL) and AST-VII (2-5 µM) for 24 hours. After treatment period, 20 µL of MTT solution at a concentration of 0.5 mg/mL was added to each well in 96-well plates; and the cells were incubated for 3 hours. Then, 200 µL of DMSO was added to each well to dissolve the formazan crystals. Finally, the absorbance values were measured using a spectrophotometer at 565 nm and 650 nm. The acquired data was statistically analyzed with GraphPad Prism to determine relative cell viabilities.

2.2.9. Chemotaxis Assay within Chemotaxis Microfluidic Device (CMD)

CMDs were used to co-culture DCs and B16-F10 cells for the investigation of small molecule induced chemotaxis of DCs towards B16-F10 cells. To confirm the stimulation dependant migration of DCs, we designed an experimental plan (Figure 2.4), including (i) treated-DCs vs None (absence of B16-F10 cells), (ii) non-treated-DCs vs B16-F10 cells, and (iii) treated-DCs vs B16-F10 cells.

For this purpose, DCs and B16-F10 cells were first stained with a green fluorescence tracker CytoTrack™ Green and a red fluorescence tracker CytoTrack™ Red (by following the manufacturer's protocol)[151,152]. Then, fluorescence-stained DCs and B16-F10 cells were seeded into CMD; and the migration of DCs towards to B16-F10 cells were monitored through fluorescence microscope.

For fluorescence staining of DCs, DCs (2×10^5 cells/well) were seeded into 24-well plate, and incubated for overnight. Next day, DCs were co-treated with LPS (100 ng/mL) and AST-VII (5 μM) for their maturation for 24 hours. Then, 100 μL of green tracking dye solution was added into wells; and the cells were incubated for 30 minutes. For fluorescence staining of B16-F10 cells, B16-F10 cells (10^5) were seeded into a 24-well plate and incubated overnight. The next day, 20 μL of red tracking dye solution was added into wells; and the cells were incubated for 1 hour. Lastly, the cells were gently washed with dPBS and detached using trypsinization.

After staining, 60 μL of B16-F10 cells (10^4 cells) were seeded into the bottom lateral channel in CMDs and incubated for 6 hours, allowing their attachment to the PMMA substrate. After 6 hours, 66 μL of LPS and AST-VII-treated DCs (2×10^4 cells) were seeded into the top lateral channel in CMDs (Figure 2.4C). The chemotaxis of mDC2.4 towards B16-F10 murine melanoma cells was observed under a fluorescent microscope (ZEISS Axio Vert.A1) for 24 hours.

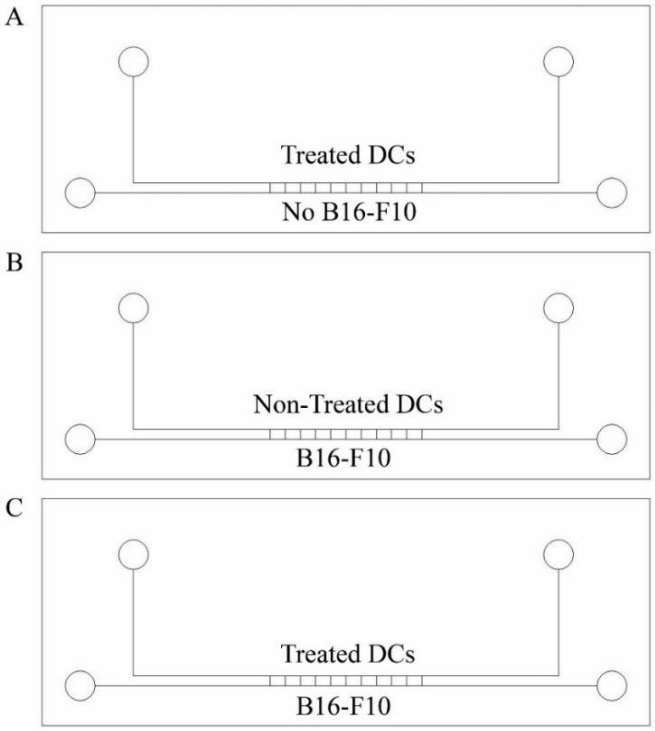

Figure 2.4. Chemotaxis assay in CMD. (A) Chemotaxis of treated-DCs in the absence of B16-F10 cells, (B) Chemotaxis of non-treated-DCs towards B16-F10 cells, and (C) Chemotaxis of treated-DCs towards B16-F10 cells.

CHAPTER 3

RESULTS AND DISCUSSIONS

3.1. Design of Chemotaxis Microfluidic Device

The Chemotaxis Microfluidic Device (CMD) was designed using AutoCAD and fabricated through laser ablation. As CMDs were designed for co-culturing DCs and B16-F10 cells, it contained top and bottom lateral channels for each cell line and also the centrally located microchannels to investigate immune-cancer cell interactions. The CMD was designed as a three-layered microfluidic device consisting of the top, middle, and bottom layers. While the top layer consisted of inlets and outlets, the middle layer was patterned with lateral channels and chemotaxis microchannels (Figure. 2.1). As this CMD design provides the possibility for real-time and single-cell tracking, it offers durability for the characterization of immune cell chemotaxis. Also, such a design was preferred instead of a Y-shaped microfluidic device because Y-shaped microfluidic devices require complex setups to deliver stable gradients. On the other hand, Y-shaped microfluidic devices are commonly utilized for adherent cells; however, loosely adherent DCs were studied in this thesis study[153].

In CMD, the widths of the top and bottom lateral channels were designed as 1000 µm to provide a low resistance path for fluid flow similar to Davidson *et al.*[154], allowing rapid equilibrium in a case of uneven filling in the inlets[154]. Moreover, the length of the centrally located microchannels was set to be a minimum of 650 µm as the laser hindered the fabrication of lower lengths deforming the carved structures. Therefore, obtaining as low as 200 µm length microchannels from Parlato *et al.*[146] was inadvisable. Microchannel depth was designed as 150 µm to have an adequate cross-section for DCs to migrate through to the B16-F10 bottom channel, preventing any backflow of melanoma cells and media to the DC top channel.

3.2. Fabrication and Characterization of Chemotaxis Microfluidic Device

The CMD was fabricated through laser ablation via Makeblock CO_2 laser cutter that provides two operation modes, vector and raster. For each mode, Power (P) and Speed (S) values were validated. Then, CMD layers were assembled before the characterization of CMDs. In addition to the structural characterization (width and depth values) of microfluidic channels in the CMD by microscope, liquid handling capacity and mechanical properties of CMDs were also determined by leakage and tensile tests, respectively. This characterization was crucial to guarantee (i) no leakage in CMD and (ii) permanent bonding between CMD layers. Firstly, the vector operation mode was validated for a pool of eighty combinations of P and S values, and the P-S combination that successfully cut 1-mm PMMA was determined. As shown in Figure. 3.1, ten combinations of P-S combinations, P40S10, P50S10, P60S10, P70S10, P80S10, P80S20, P90S10, P90S20, P100S10, and P100S20, could successfully cut the 1 mm thick PMMA.

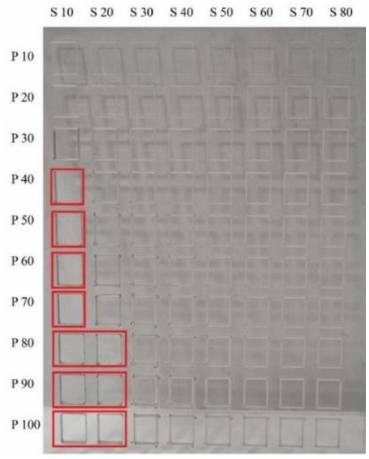

Figure 3.1. Fabrication P and S combinations that cut the 1 mm thick PMMA sheet using the vector mode depicted under red rectangles.

Furthermore, the errors for ten P-S combinations in vector mode were determined. For this purpose, five different rectangles with varied width values (500, 700, 800, 900, and 1000 μm) were cut through vector mode. Then, images were taken by microscope (Figure. 3.2). After that, the width values were measured from each image using Zen Blue

software (Table 3.1). At the end, the obtained width values were compared with theoretical width values. Then the error percentages for each P-S combination were determined (Figure. 3.3). It was shown that (i) the obtained values were higher than theoretical values, (ii) the error percentages increased by an increment of P values at a constant speed; and (iii) the error percentages decreased by an increment of S values at a constant power. For the 500 μm of theoretical width, the lowest and highest error rates were recorded as 29.36% and 46.47% by P40S10 and P100S10, respectively. For the 700 μm of theoretical width, the lowest and highest error was 17.85% and 37.67% by P80S20 and P100S10, respectively. For the 800 μm of theoretical width, the lowest and highest error rate was 14.30% and 35.95% by P80S20 and P100S10, respectively. For the 900 μm of theoretical width, the lowest and highest error rates were 14.65% and 35.08% by P80S20 and P100S10, respectively, yielding an average width of 1031.89 and 1215.69 μm, respectively. For the 1000 μm of theoretical width, the lowest and highest error rates were 17.32% and 26.42% by P40S10 and P90S10, respectively (Figure. 3.3).

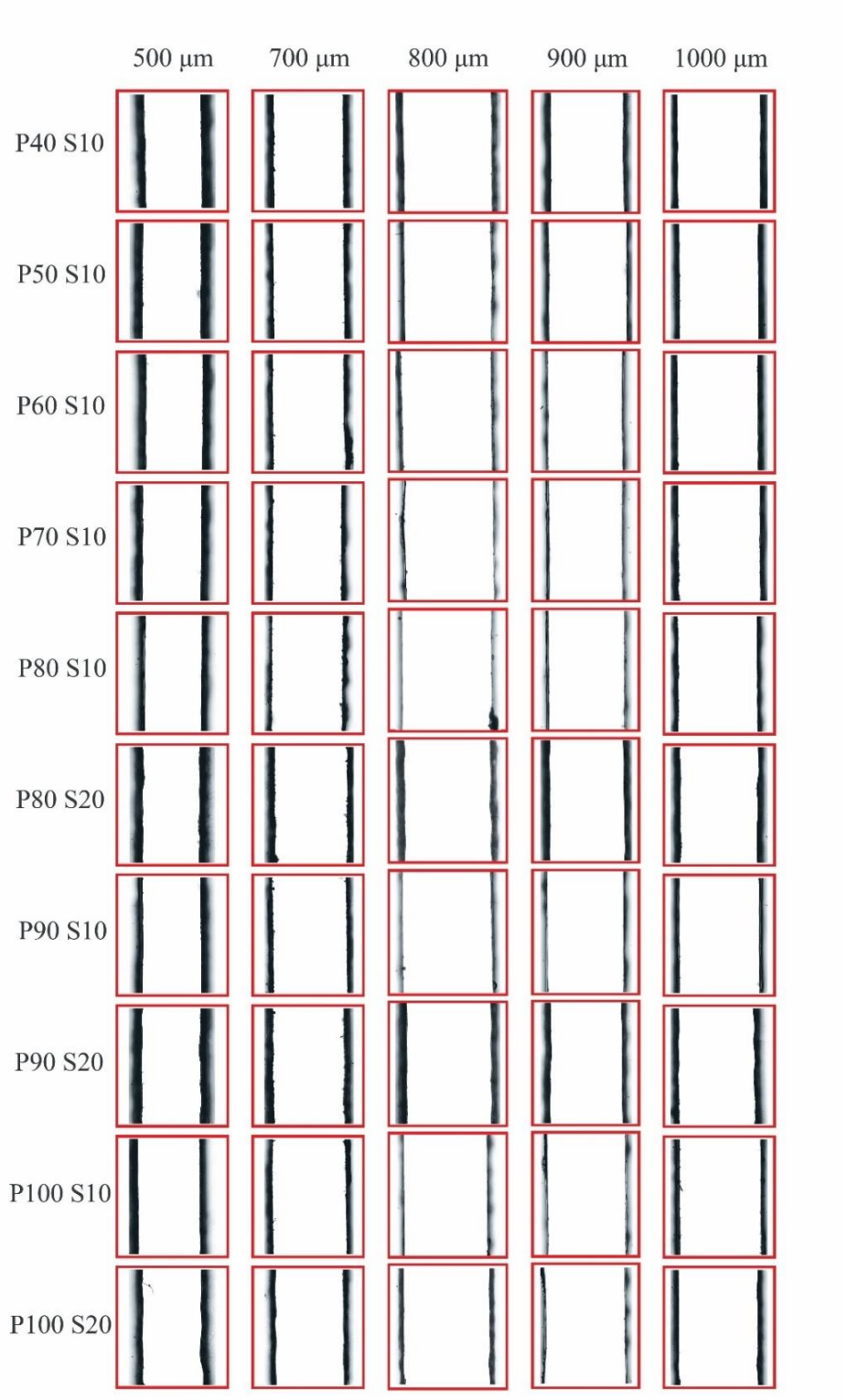

Figure 3.2. Microscopic images of obtained microfluidic channels by ten parameters used in vector mode operation.

Table 3.1. Average width values obtained by vector mode operation.

P - S Combinations	Average Width (µm)				
	500 µm	700 µm	800 µm	900 µm	1000 µm
P40S10	646.8 ± 9.8	861.2 ± 9.4	963.4 ± 11.1	1075.5 ±17.7	1173.2 ± 39.7
P50S10	664.2 ± 14.4	901.6 ± 12.6	1026.3 ± 8.3	1106.1 ± 6.5	1200.9 ± 10.5
P60S10	689.5 ± 8.6	912.2 ± 14.0	1020.4 ± 12.7	1144.5 ± 25.6	1202.7 ± 38.6
P70S10	711.9 ± 19.8	925.5 ± 21.7	1052.2 ± 19.3	1147.8 ± 8.6	1217.9 ± 15.2
P80S10	713.4 ± 16.0	945.7 ± 5.6	1074.6 ± 17.9	1179.0 ± 21.4	1251.3 ± 28.6
P80S20	615.7 ± 9.7	824.9 ± 8.9	914.5 ± 6.8	1031.9 ± 17.9	1151.9 ± 21.6
P90S10	720.5 ± 8.3	946.9 ± 16.7	1079.7 ± 12.9	1164.6 ± 4.9	1264.2 ± 32.3
P90S20	616.5 ± 8.7	853.3 ± 26.5	989.0 ± 7.0	1079.0 ± 13.1	1166.1 ± 48.6
P100S10	732.3 ± 7.7	963.7 ± 6.6	1087.6 ± 13.5	1215.7 ± 28.7	1255.4 ± 32.7
P100S20	670.9 ± 11.3	871.1 ± 15.4	1056.8 ± 5.7	1180.1 ± 20.2	1179.3 ± 12.7

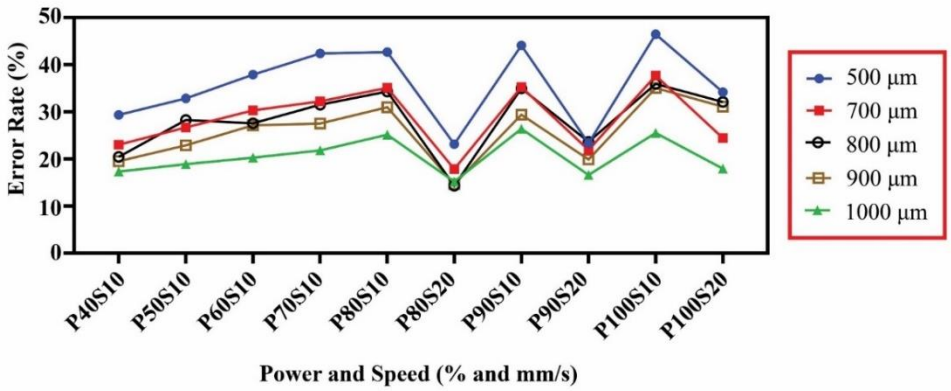

Figure 3.3. Error rates for ten different P-S combinations in vector operation mode. Each data point represents the percentage difference between obtained width and the theoretical width.

As a result, P80S20 ensured the lowest error rate in vector mode. Using the data obtained from P80S20, an equation showing how much should be drawn to obtain an exact width value (1000 µm) for the CMD lateral channels was designed. Figure 3.4 shows the graph obtained by plotting theoretical vs obtained width values. Also, it shows an equation that was used to calculate how much width should be drawn to obtain 1000 µm of width using vector mode with P80S20. Accordingly, it was noted that due to an increase in length after vector mode ablation, the two lateral channels should be drawn 866.86 µm apart obtaining a final distance of 1000 µm as a width for the fabrication of CMD lateral channels.

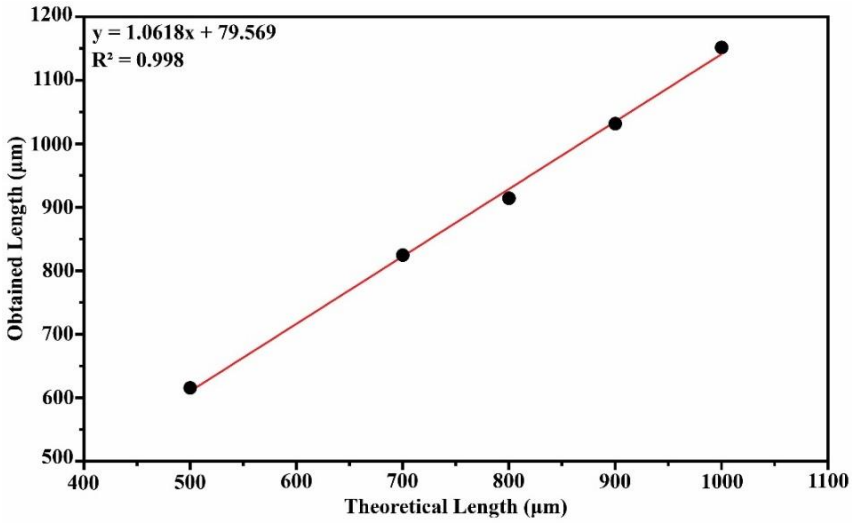

Figure 3.4. Theoretical vs. obtained width values during the vector mode operation with P80S20.

In addition to vector mode, the raster mode operation was validated by various P-S combinations. For this purpose, a 1-mm thick PMMA plate was ablated using the raster mode with eighty different P-S combinations. Then, widths and depths (µm) values of centrally located microchannels were measured. After engraving, microchannels were observed under a microscope (Figure. 3.5). Microchannels' average width and depth (µm) values were then measured using the images taken from a microscope.

According to data obtained, the widths of engraved microchannels decreased with an increasing S value at a constant P value (Figure. 3.6). While the maximum width was obtained as 446.8 ± 12.3 µm by P90S10, P10S80 provided the minimum width as 136.2 ± 11.8 µm. Also, with an increasing P value at constant S, the width dimension tends to increase; for example, when speed is kept constant at the value of 10 mm/s, the width for P10S10 is 246.2 ± 32.3 µm, and the width for P100S10 is 402.6 ± 8.5 µm. Moreover, with an increasing S at constant P, the width value of microchannels decreased (Figure. 3.6). For example, the width obtained by P50S10 was 392.3 ± 5.3 µm; however, it significantly reduced to 268.7 ± 6.8 µm (P50S80) by increasing the S value in raster mode. According to the obtained data, it can be concluded that (i) P increase at constant S causes the increase in the width values, and (ii) S increase at constant P provides microchannels with smaller width values (Table 3.2).

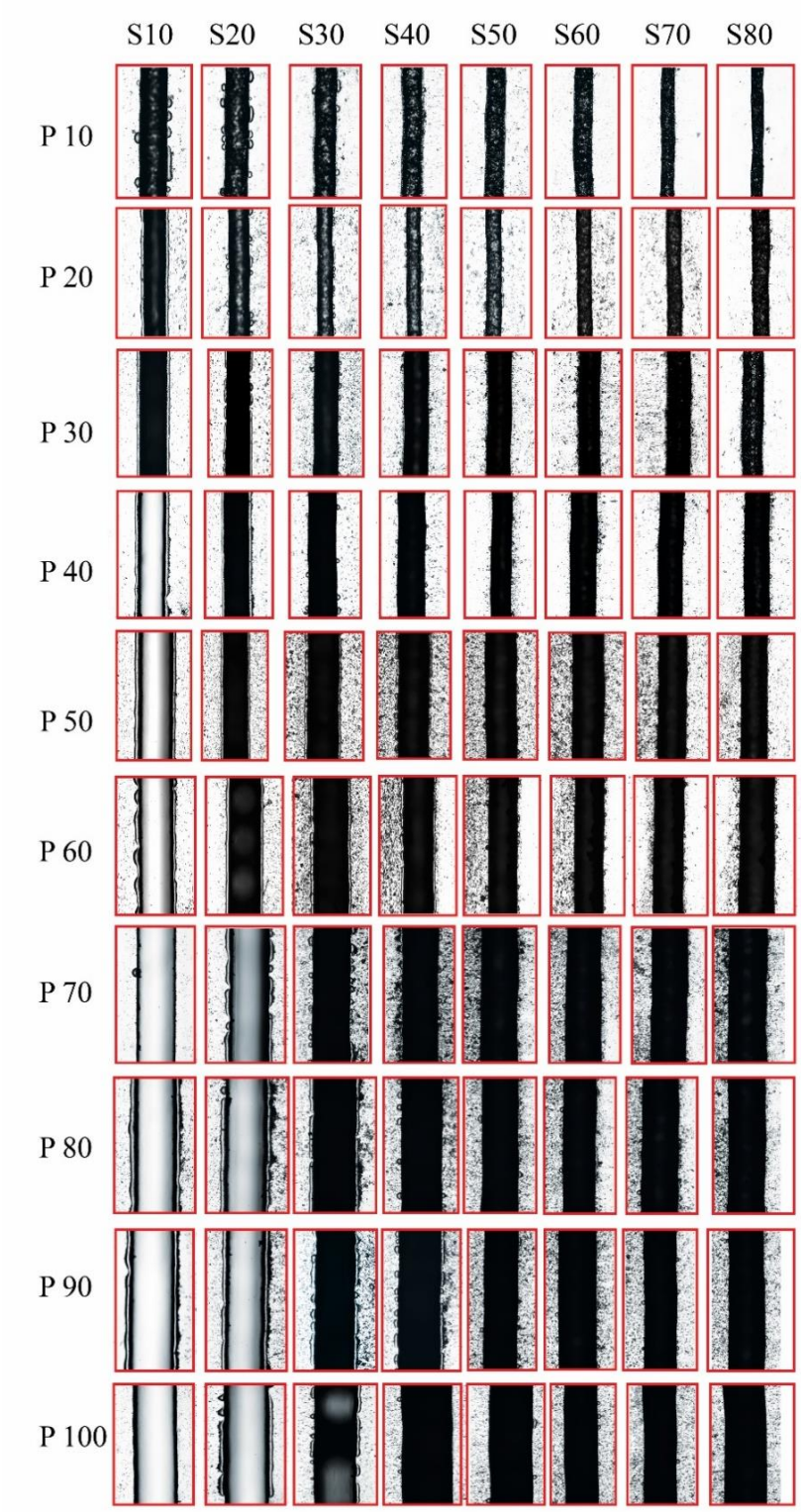

Figure 3.5. Microscopic images of centrally located microchannels obtained by raster mode operation through eighty different P-S combinations.

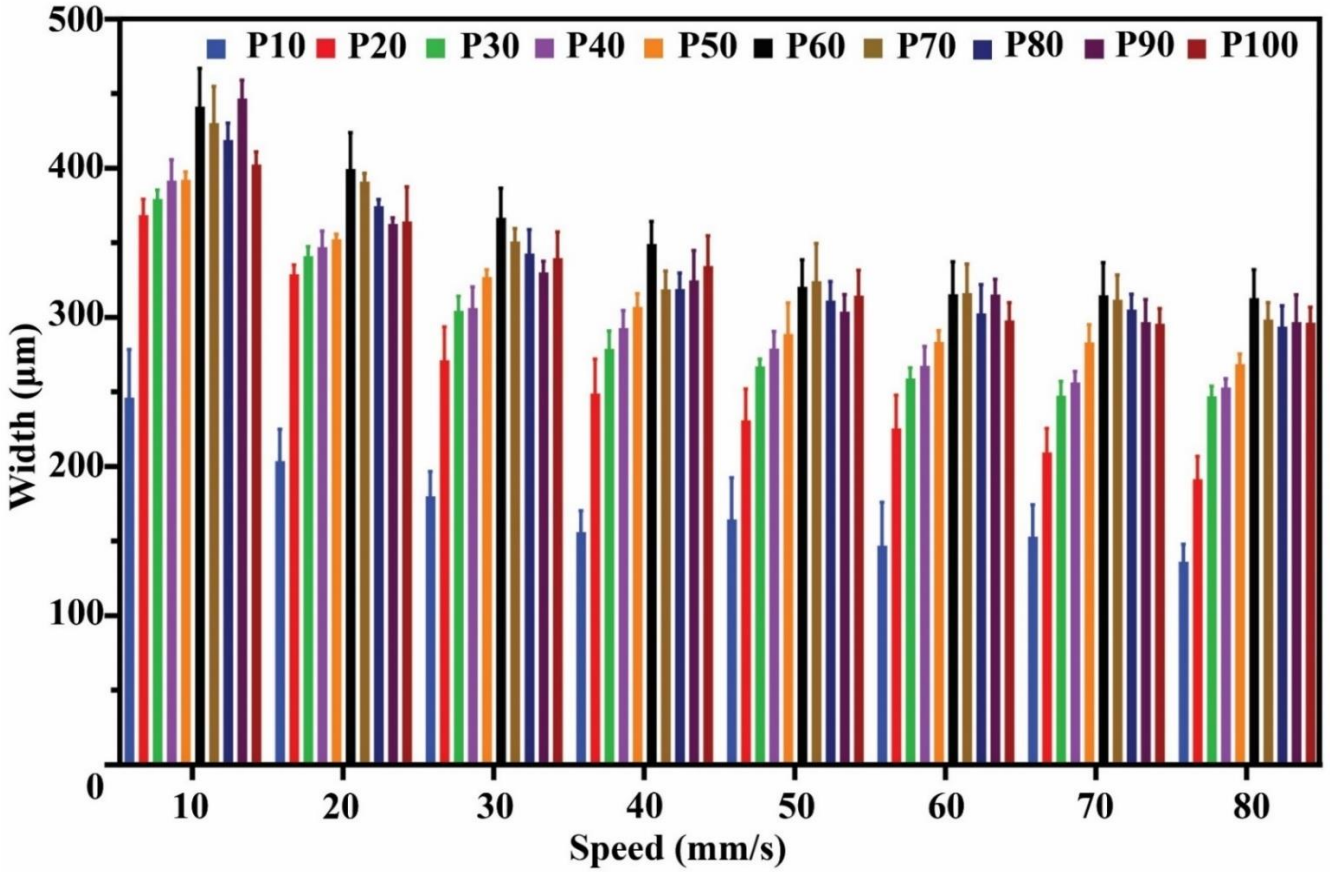

Figure 3.6. The width values of centrally located microchannels on the PMMA plate using eighty P-S combinations. The bars in the bar graph represent the average of three independent experiments, and the error bars indicate the standard deviation.

Table 3.2. Average widths (μm) of microchannels obtained by raster mode.

Speed (mm/s)	Power (%)									
	10	**20**	**30**	**40**	**50**	**60**	**70**	**80**	**90**	**100**
10	246.2 ± 32.3	368.6 ± 10.6	379.4 ± 6.1	391.8 ± 14.1	392.3 ± 5.3	441.3 ± 25.8	430.4 ± 24.4	419.0 ± 11.2	446.8 ± 12.3	402.6 ± 8.5
20	203.7 ± 21.4	302.4 ± 6.2	341.2 ± 6.4	347.3 ± 10.7	352.5 ± 3.3	399.6 ± 24.4	391.1 ± 5.6	374.5 ± 4.6	362.7 ± 4.2	364.4 ± 23.2
30	180.0 ± 16.4	271.3 ± 22.4	304.5 ± 9.8	306.4 ± 14.1	327.2 ± 4.9	366.8 ± 19.9	350.9 ± 8.7	342.8 ± 16.0	330.1 ± 7.7	339.7 ± 17.6
40	156.0 ± 14.4	249.1 ± 23.1	278.9 ± 12.1	293.0 ± 11.7	307.2 ± 8.7	349.3 ± 15.1	318.8 ± 12.2	318.9 ± 10.8	324.9 ± 20.1	334.4 ± 20.4
50	164.6 ± 27.9	231.1 ± 21.0	267.2 ± 5.0	279.1 ± 11.5	289.0 ± 20.8	320.5 ± 18.2	324.4 ± 25.3	311.2 ± 13.0	303.9 ± 11.4	314.6 ± 17.1
60	147.1 ± 29.0	225.7 ± 22.3	259.1 ± 7.1	267.5 ± 13.0	283.6 ± 7.7	315.6 ± 21.8	316.3 ± 19.5	302.7 ± 19.2	315.5 ± 10.1	298.1 ± 11.8
70	153.0 ± 21.3	209.5 ± 16.2	247.6 ± 9.6	256.4 ± 7.4	283.3 ± 11.9	314.9 ± 21.9	311.8 ± 16.7	305.3 ± 10.3	297.0 ± 15.1	295.8 ± 10.3
80	136.2 ± 11.8	191.6 ± 15.3	247.2 ± 6.9	253.1 ± 5.8	268.7 ± 6.8	313.0 ± 19.0	298.5 ± 11.4	293.8 ± 14.1	296.8 ± 18.4	296.5 ± 10.5

In addition to the analysis of width values, the effects of P-S on the depth of microchannels were investigated. For this purpose, the PMMA plate was engraved using raster mode with eighty different P-S combinations again. Then, it was placed vertically on the microscope stage to obtain depth images (Figure. 3.7). Moreover, the depth values of each microchannel were determined as previously done for width analysis.

As shown in Figure. 3.8, the depth of microchannels decreased by increasing S at a constant P value. For instance, the depth value was recorded as 446.0 ± 24.3 μm for P30S10; however, it was obtained as 91.8 ± 24.1 μm for P30S80. We also realized that the depth value increased when P was increased at a constant S value. For example, the depths of the microchannel were 22.9 ± 6.0 and 644.6 ± 30.8 μm for P20S50 and P90S50, respectively. Moreover, several P-S combinations in raster mode operation completely cut 1-mm PMMA, such as P40S10, P50S10, P60S10, P70S10-20, P80S10-20, P90S10-20, and P100S10-30. Interestingly, some P-S combinations could not create microchannels, including P10S40-80 and P20S60-80 (Table 3.3).

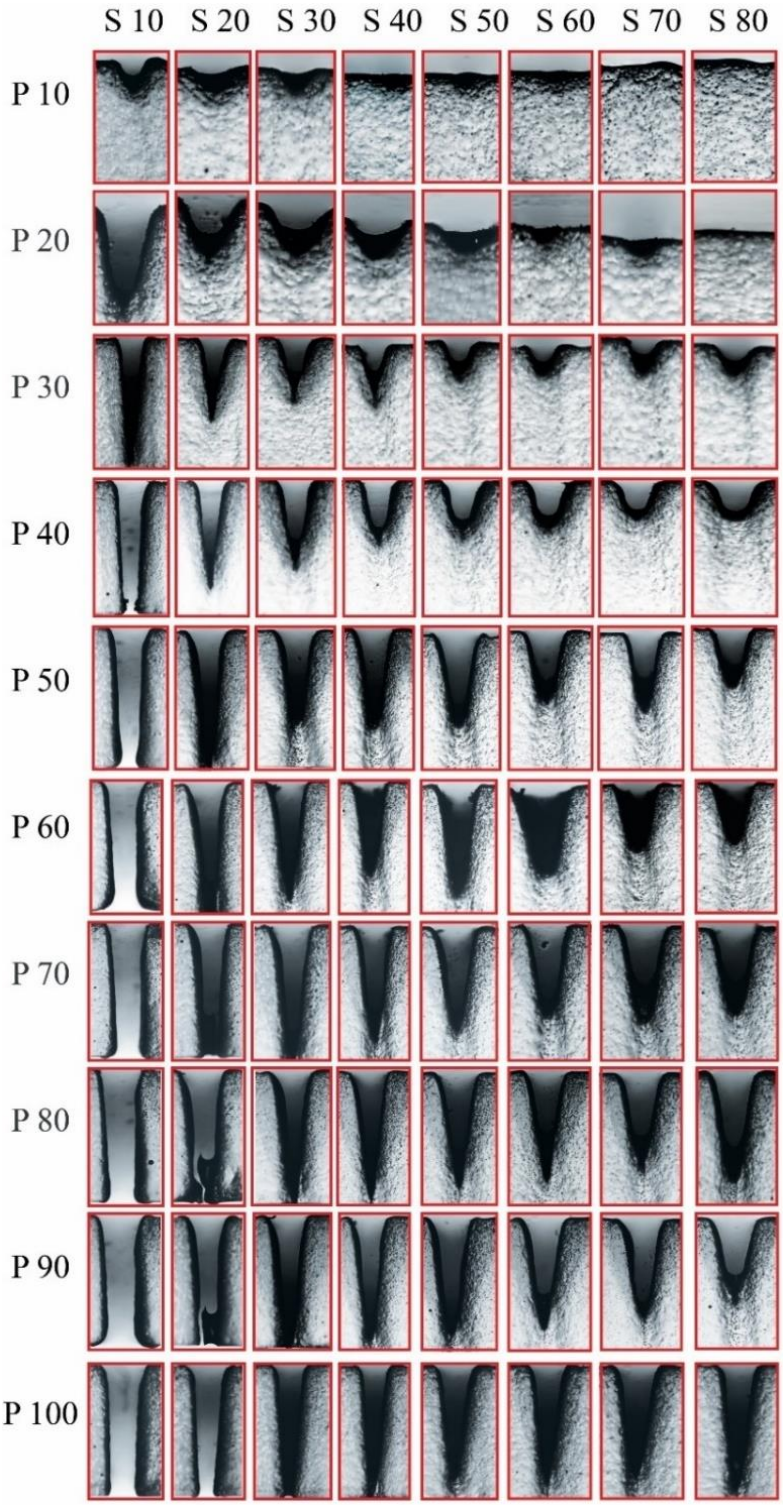

Figure 3.7. Microscopic images of rasterized PMMA plate for analysis of depth values.

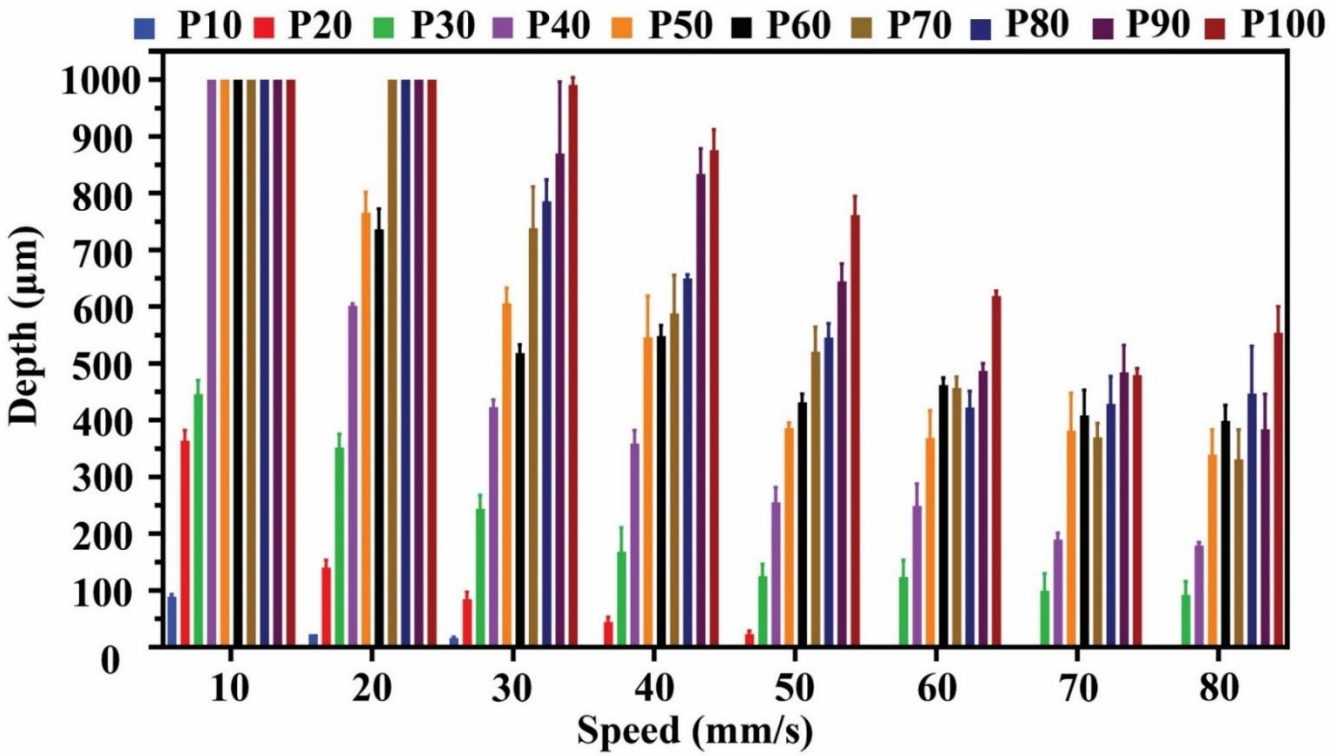

Figure 3.8. The depth values of centrally located microchannels on the PMMA plate using eighty P-S combinations. The bars in the bar graph represent the average of three independent experiments, and the error bars indicate the standard deviation.

Table 3.3. Average depths (μm) of microchannels obtained by raster mode operation in eighty different P-S combinations. While some of the P-S combinations cut completely 1-mm PMMA plate (>1 mm), some of them could not ablate (Not A), resulting in no depth.

Speed	**Power (%)**									
(mm/s)	**10**	**20**	**30**	**40**	**50**	**60**	**70**	**80**	**90**	**100**
10	88.8 ± 4.2	364.0 ± 17.8	446.0 ± 24.3	>1 mm	>1 mm	>1 mm	>1 mm	>1 mm	>1 mm	>1 mm
20	23.2 ± 0.1	147.6 ± 1.9	351.7 ± 23.9	601.6 ± 3.4	765.5 ± 35.9	736.1 ± 36.5	>1 mm	>1 mm	>1 mm	>1 mm
30	16.1 ± 1.8	84.7 ± 12.5	243.6 ± 24.1	423.0 ± 13.2	605.5 ± 27.3	518.1 ± 14.9	762.9 ± 36.0	785.7 ± 38.1	808.8 ± 61.1	>1 mm
40	Not A	44.4 ± 8.6	168.1 ± 42.3	358.8 ± 23.3	541.2 ± 32.9	548.0 ± 19.3	591.0 ± 57.0	649.7 ± 7.0	833.8 ± 44.8	875.8 ± 36.1
50	Not A	22.9 ± 6.0	125.2 ± 21.2	255.2 ± 26.8	386.2 ± 9.3	431.2 ± 15.0	520.6 ± 43.5	545.8 ± 24.3	644.6 ± 30.8	761.2 ± 33.4
60	Not A	Not A	123.9 ± 29.7	248.8 ± 38.9	368.3 ± 48.6	461.5 ± 13.2	456.8 ± 19.3	421.9 ± 29.2	487.1 ± 13.0	618.6 ± 9.2
70	Not A	Not A	99.7 ± 29.9	189.3 ± 11.7	307.2 ± 1.9	408.0 ± 45.0	369.5 ± 25.1	428.4 ± 48.6	484.6 ± 47.4	479.5 ± 11.5
80	Not A	Not A	91.8 ± 24.1	1179.2 ± 5.6	350.2 ± 8.7	398.9 ± 27.3	301.1 ± 15.5	342.5 ± 20.6	383.9 ± 61.8	554.1 ± 45.8

According to the CMD design (Figure 2.1), the required widths and depths of centrally located chemotaxis microchannels should be 300 and 150 μm, respectively. As shown in Table 3.3, P20S20 offered a microfluidic channel with 302.4 ± 40.3 μm of width and 140.3 ± 13.2 of depth. Therefore, P20S20 was chosen for raster mode to fabricate centrally located microchannels in CMDs.

In conclusion, P-S combinations were validated for the vector and raster mode operation modes in laser ablation. For the vector mode, P80S20 was termed the optimal P-S combination due to its lowest error rate. However, P20S20 was determined as an optimal P-S combination since it offered the required width and depth values for centrally located microfluidic channels.

After accomplishing the P-S optimization of both operation modes, each layer was fabricated (Figure 3.9) and assembled to fabricate CMD using two independent assembly techniques.

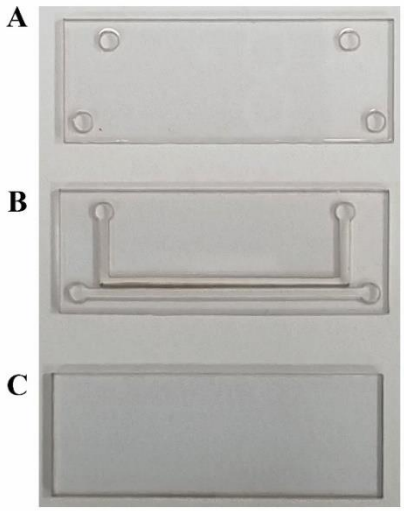

Figure 3.9. Individual layers of the CMD fabricated using determined P-S combination. (A) Top layer containing the inlets and outlets, (B) Middle layer with lateral channels and microchannels, (C) Bottom layer as support.

Assembly technique one (AT 1) employed adhesive bonding to assemble the CMD layers. A double-sided adhesive tape was placed on both sides of the middle layer for adhesive bonding. However, the P80S20 combination could not ablate the 1-mm PMMA by vector mode. This limitation led to the utilization of Assembly Technique two (AT 2), which was thermally-assisted solvent bonding to assemble each layer of CMDs.

For thermally-assisted solvent bonding, ethanol (EtOH) and isopropyl alcohol (IPA) were utilized to provide permanent bonding between the CMD layers. The bonding conditions for each solvent were varied in terms of solvent concentration, bonding temperature, and incubation time (**Table 3.4**). We noticed that CMD layers could not bind each other permanently at lower concentrations of solvents (50%). However, the permanent bonding of CMD layers was observed when solvents were used at 80% concentration regardless of incubation temperature and time. These results recapitulated previous findings by Bamshad *et al.* where PMMA substrate bonding is reversible (partially bonded) and irreversible (fully bonded) at 50 % and 80 % EtOH and IPA concentrations, respectively[155]. The assembled CMDs with any deformation or cracking are shown in **Figure. 3.10** and **Figure 3.11** for CMDs assembled with EtOH and IPA, respectively.

Table 3.4. CMD layers were assembled via ethanol (EtOH) and isopropyl alcohol (IPA).

Solvent Concentration	Temperature	Time (minutes)	Bonding Result	
			EtOH	IPA
50%	60°C	5	Fail	Fail
		10	Fail	Fail
		20	Fail	Fail
	70°C	5	Fail	Fail
		10	Fail	Fail
		20	Fail	Fail
60%	60°C	5	Fail	Fail
		10	Fail	Fail
		20	Fail	Success
	70°C	5	Fail	Fail
		10	Fail	Success
		20	Success	Success
70%	60°C	5	Fail	Fail
		10	Fail	Fail
		20	Success	Success
	70°C	5	Fail	Fail
		10	Success	Success
		20	Success	Success
80%	60°C	5	Success	Success
		10	Success	Success
		20	Success	Success
	70°C	5	Success	Success
		10	Success	Success
		20	Success	Success

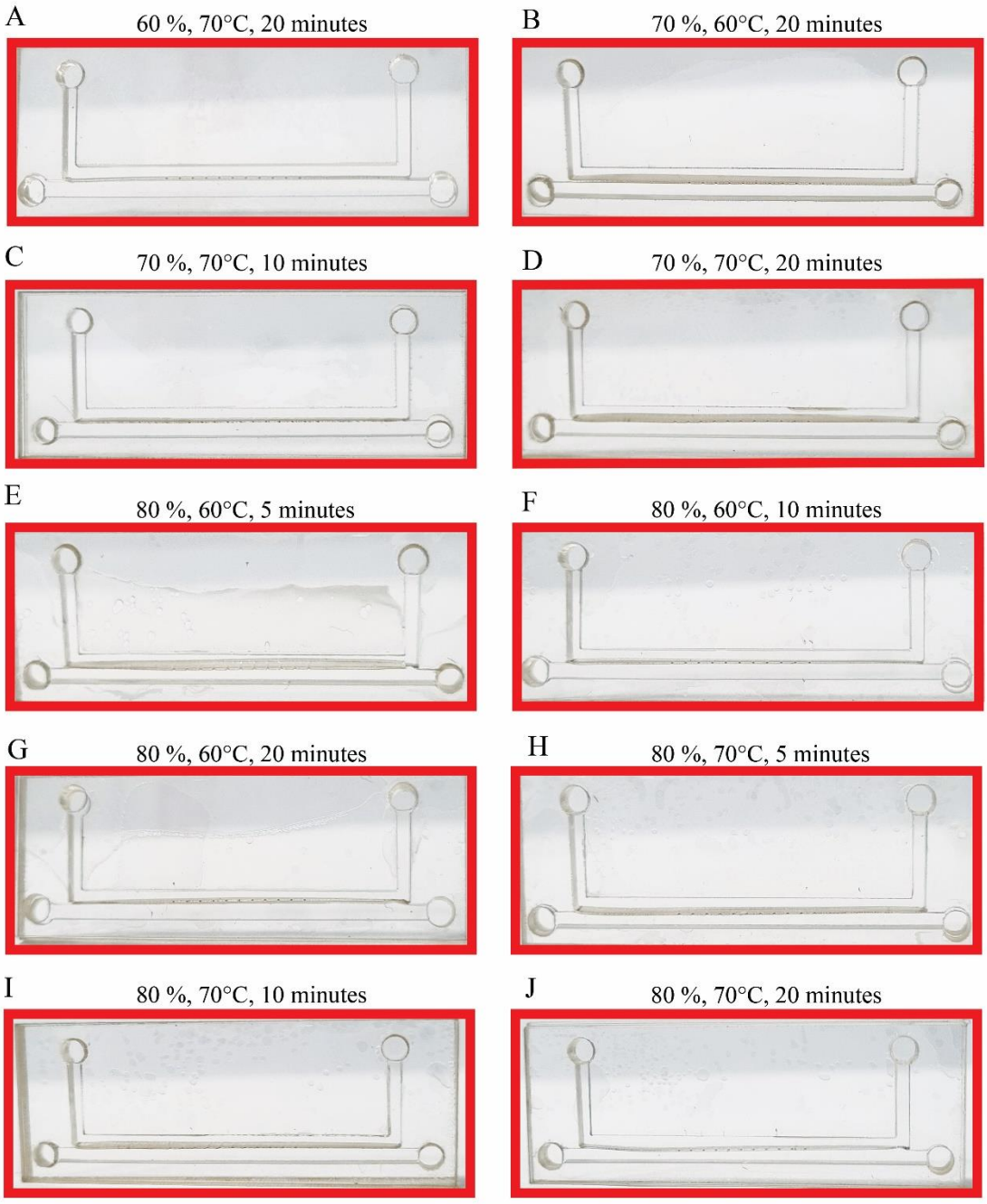

Figure 3.10. Three-layered CMDs were assembled using ethanol at various incubation temperatures and times.

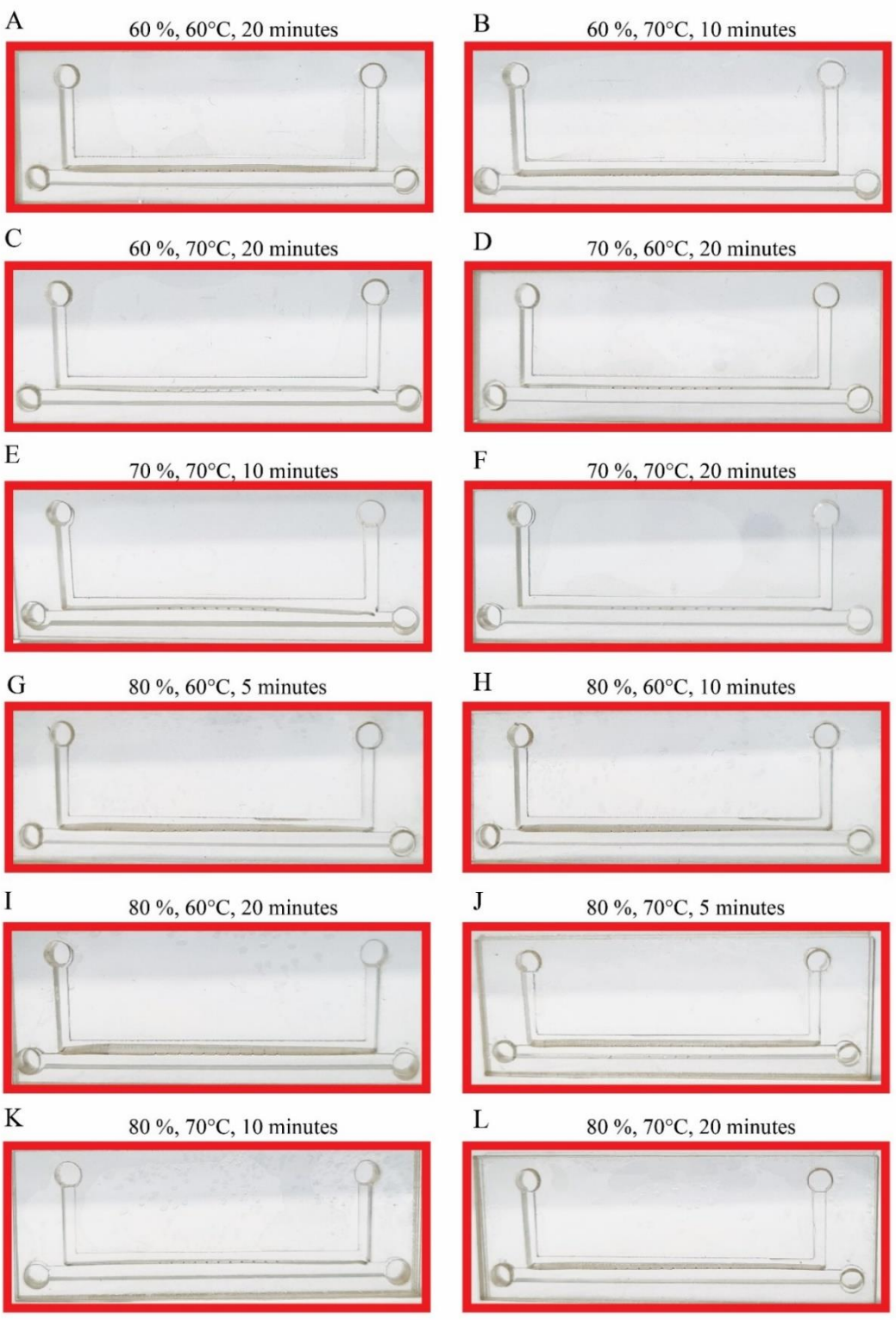

Figure 3.11. Three-layered CMDs were assembled using isopropyl alcohol at various incubation temperatures and times.

Moreover, leakage tests characterized the CMDs in terms of their liquid handling capacity. Principally, leakage tests were conducted by pipetting a blue ink dye into the lateral channels to observe potential bleeding to confirm which bonding condition was efficient in terms of permanent bonding. Figure. 3.12 and Figure. 3.13 shows the efficacy of the thermally-assisted solvent bonding technique on the assembly of CMD layers using ethanol and isopropyl alcohol, respectively. We observed the leakage in CMDs assembled using 60% EtOH and IPA. Also, samples leaked from the microchannels in CMDs assembled using 70% concentration of solvents at 60°C and 70°C. Moreover, CMDs assembled using an 80% concentration of both solvents at 60°C caused the leakage of liquid samples in microchannels. However, no sign of liquid leakage in CMDs assembled using an 80% concentration of both solvents at 70°C (Figure. 3.12-13). As a result, eight and nine of the assembly conditions from the ethanol and isopropyl alcohol groups show leaks, respectively. A total of five bonding conditions showed no visual leaks.

Later, CMDs that were permanently assembled (non-leaked CMDs - five conditions) were subjected to mechanical tensile testing to determine their maximum tensile strengths. For that purpose, Force (kN) and stroke (mm) were obtained for each CMD, and then the stress and strain values were calculated. Using stress and strain values, the maximum tensile strength for each CMD was determined (Table 3.5). We could not see significant differences in the bonding strengths of CMDs assembled using EtOH for 10 and 20 minutes. The values of bonding strengths were determined as 22.2 to 22.4 MPa. However, the bonding strengths of CMDs assembled using isopropyl alcohol differed depending on the incubation time. As shown in Table 3.5, the bonding strengths were determined as 19.2 and 22.3 MPa for 5 and 20 minutes, respectively. Overall, both solvents at 80% concentration offered comparable tensile strengths, especially for long incubation times.

Due to leakage and tensile testing, the optimal assembly condition for CMD layers was established by using 80% ethanol at 70°C for 20 minutes, resulting in high bonding strength without any leakage.

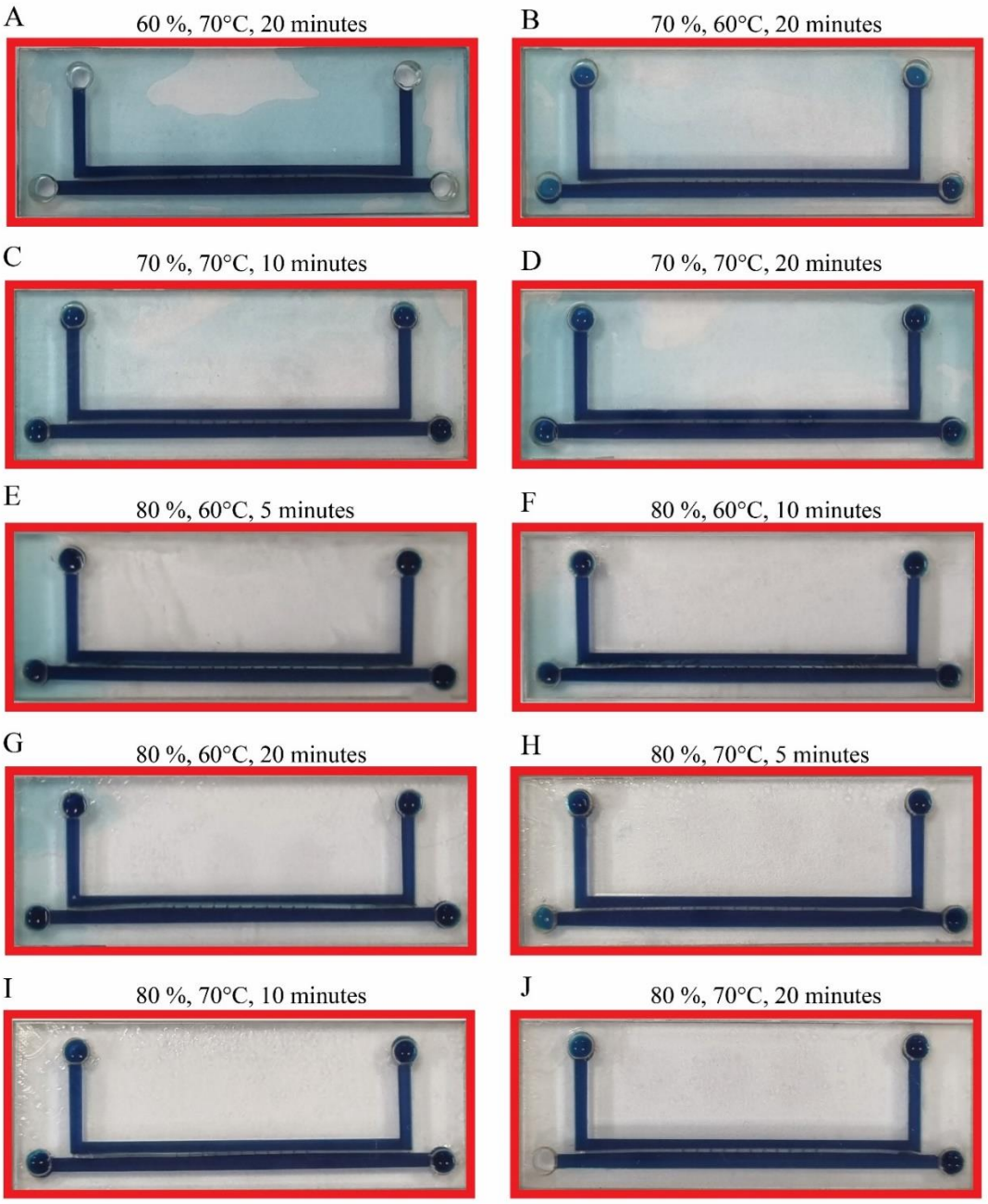

Figure 3.12. Leakage tests for CMDs assembled using ethanol.

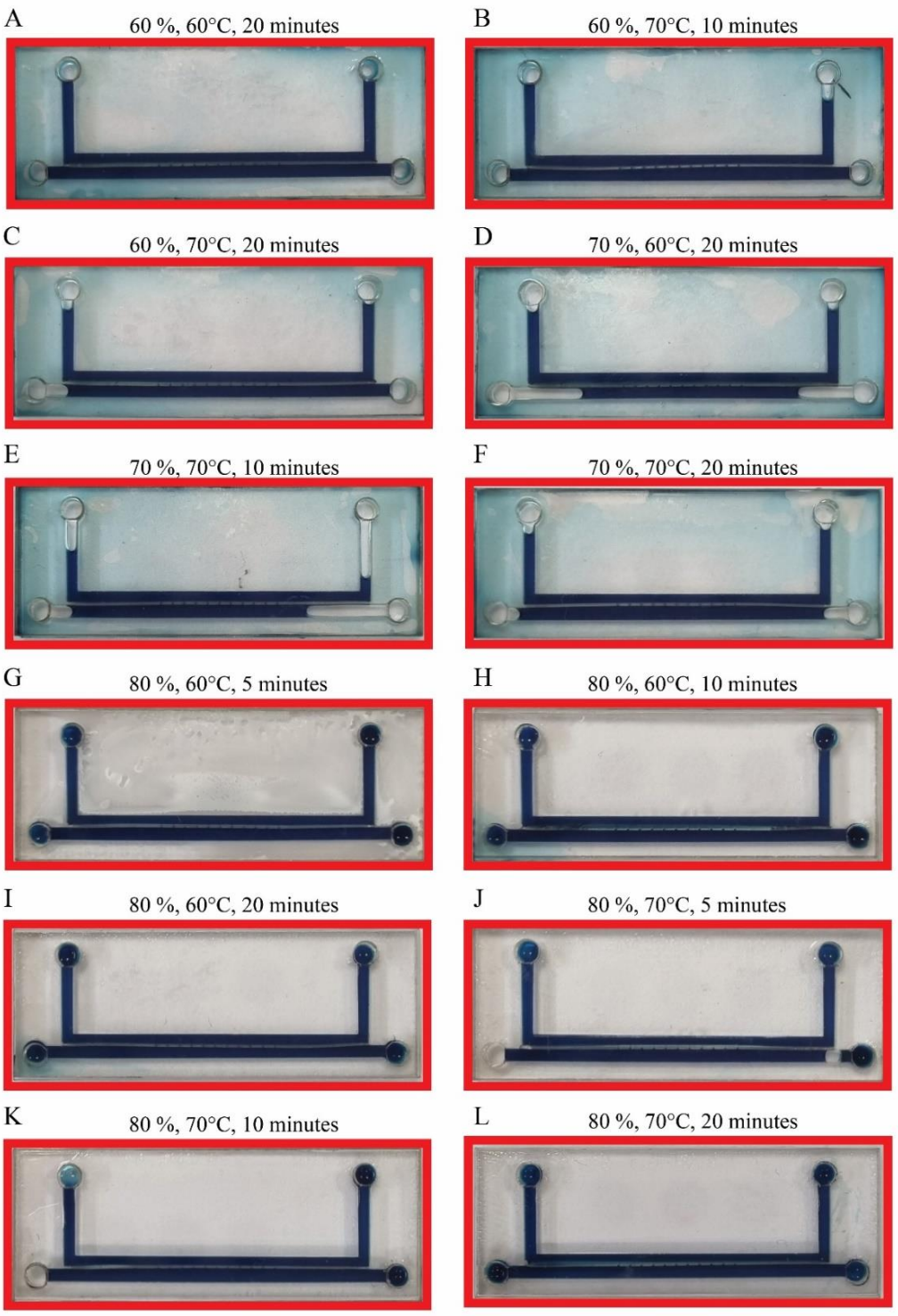

Figure 3.13. Leakage tests for CMDs assembled using isopropyl alcohol.

Table 3.5. Maximum tensile strength of CMDs assembled using ethanol and isopropyl alcohol at various incubation temperatures and times.

Solvent	Solvent Concentration	Incubation Temperature	Incubation Time	Bonding Strength (MPa)
Ethanol	80%	70°C	10 min	22.2
			20 min	22.4
Isopropyl Alcohol	80%	70°C	5 min	19.2
			10 min	19.5
			20 min	22.3

3.3. Validation of CMDs for Cell Culture Studies

The CMD was evaluated in terms of their use in cell culture studies after fabrication. Before culturing cells into the CMD, fabricated CMDs were sterilized using autoclaving or UV treatment. To validate the efficacy of the sterilization techniques, the viabilities of DC2.4 dendritic (DCs) and B16-F10 melanoma cells cultured within lateral channels were determined for 48 hours using Live/Dead Assay.

In Figure 3.14, DCs showed high cell viability in either autoclaved or UV-treated CMDs for the first 24 hours. However, we observed higher cell viability in autoclaved CMDs than in UV-treated CMDs at 48 hours. In detail, the red fluorescent intensity increased in UV-treated CMDs over time, while the cells in autoclaved CMDs were kept their viabilities for 48 hours. Additionally, the higher viabilities of B16-F10 cells were observed in autoclaved CMDs compared to UV-treated CMDs for 48 hours (Figure. 3.15). Concludingly, it was noticed that sterilization through autoclaving provided the highest DCs and B16-F10 cell viability for 48 hours.

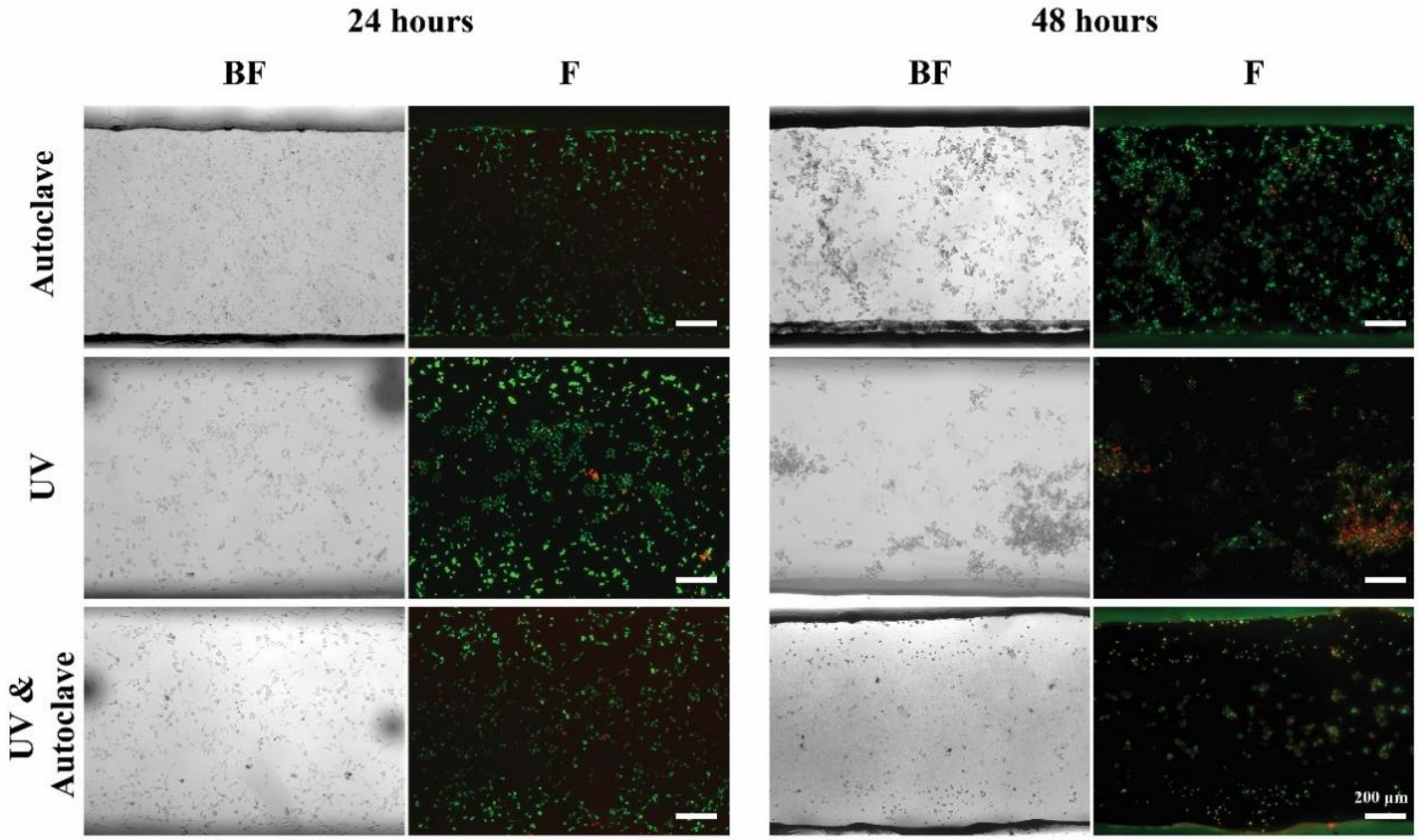

Figure 3.14. Live/Dead Assay shows the viability of DCs seeded into CMDs sterilized through (i) autoclaving, (ii) UV treatment, and (iii) autoclave and UV for 48 hours. BF: Brightfield, F: Fluorescence. The live and dead cells are exhibited in green and red fluorescence, respectively. The scale bar represents 200 µm.

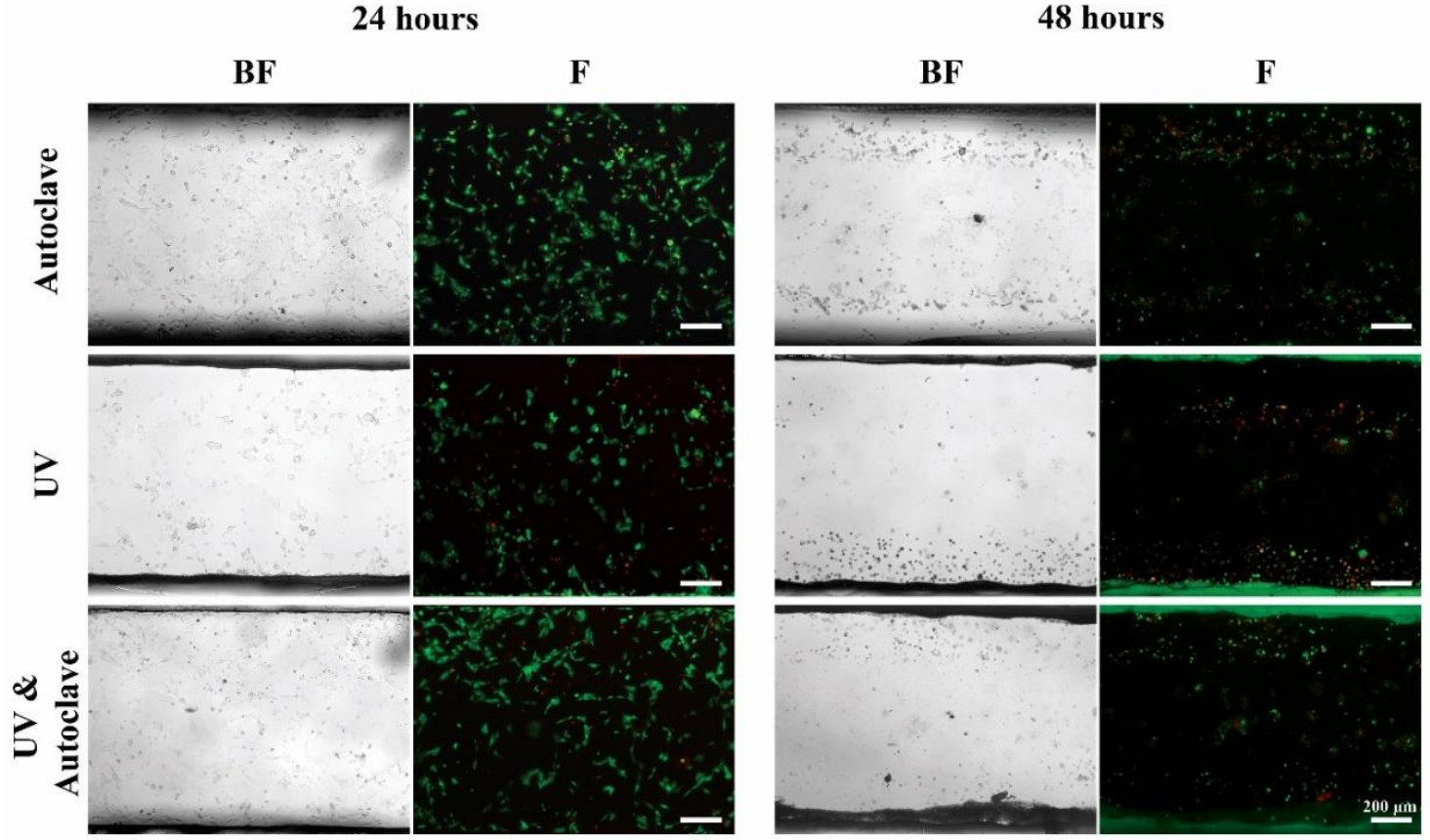

Figure 3.15. Live/Dead Assay shows the viability of B16-F10 cells seeded into CMDs sterilized using (i) autoclave, (ii) UV treatment, and (iii) autoclave and UV for 48 hours. BF: Brightfield, F: Fluorescence. The live and dead cells are exhibited in green and red fluorescence, respectively. The scale bar represents 200 µm.

3.4. Investigation of Small Molecule Induced CCR5/CCL2-CCL5 Expression on Dendritic and Melanoma Cells

Understanding the chemotactic environment of tumors and identifying chemokines that regulate immune cell migration into tumors is essential to develop immunotherapeutics[156]. In anti-tumor immunity, dendritic cells migrate into the tumor through XCR1, CCL3, CCL4, CCL5, and CCL20 present in the tumor microenvironment (TME), capturing tumor antigens and reaching a maturated state to activate T cells in lymph nodes. The secretion of chemokines, such as CCL5 for CCR5, CXCL9/10/11 for CXCR3 in the TME, is necessary for initiating a tumor-specific immune response[157]. Additionally, in melanoma, 12-chemokine signatures (CCL2, CCL3, CCL4, CCL5, CCL8, CCL18, CCL19, CCL21, CXCL9, CXCL10, CXCL11, and CXCL13) were associated with better survival of melanoma patients[158]; therefore, CCL2 and CCL5 chemokines, which are both agonist for CCR5[118] were chosen. To show the directional migration of DCs to B16-F10, whether it is guided by chemotaxis or not, the expression of the CCR5 receptor on DCs and its corresponding ligands, CCL2 and CCL5, in B16-F10, were investigated by using flow cytometry.

Previous studies on DC chemotaxis have shown differences between immature DCs and mature DCs regarding chemokine receptor expression levels. Parlato *et al.*[149] demonstrated that interferon-treated DCs (IFN-DCs) showed an elevated expression of chemokine receptor CXCR4 compared to immature DCs. Subsequently, they showed the role of the CXCR4/CXCL12 axis in the guided migration of IFN-DCs towards colorectal cancer cells[149]. According to this reference study, we aim to maturate DCs by a small molecule, Astragaloside VII (AST-VII), to investigate the expression level of CCR5 and the effect on directional migration along the CCR5/CCL2-5 axis.

As shown in previous work, Yakubogullari *et al.*[159] demonstrated that AST-VII cooperating with LPS induced the maturation and activation of mouse bone marrow-derived dendritic cells (BMDCs). As AST VII alone did not enhance dendritic cell maturation, co-treatment of AST VII with LPS increased the expression of MHCII, CD86, and CD80 on DCs and the production of pro-inflammatory cytokines such as IL-1β and IL-12[159].

In light of this information, we investigated the expression levels of CCR5 on immature and mature DCs stimulated with AST-VII and LPS. DCs were treated with AST-VII (5 μM), LPS (100 ng/mL) alone, or AST-VII (5 μM) + LPS (100 ng/mL) for 24 h. Immature dendritic cells express CCR5 receptors on their surfaces as clearly stated in literature[116,117]. As AST-VII alone did not enhance the maturation of dendritic cells[159], similar CCR5 levels were observed in AST-VII-treated dendritic cells compared to RPMI treated DCs. CCR5 expression levels on DCs significantly increased following the stimulation with LPS alone and LPS+AST-VII compared to RPMI-treated DCs, indicating dendritic cell maturation influences CCR5 expression. However, AST-VII did not alter the CCR5 expression in LPS+AST-VII treated dendritic cells over LPS alone (Figure 3.16).

These data showed that DCs in the mature state expressed higher CCR5 receptors than the immature state, demonstrating that LPS+AST VII stimulated cells could be used to guide the chemotaxis of DCs toward B16-F10 cells.

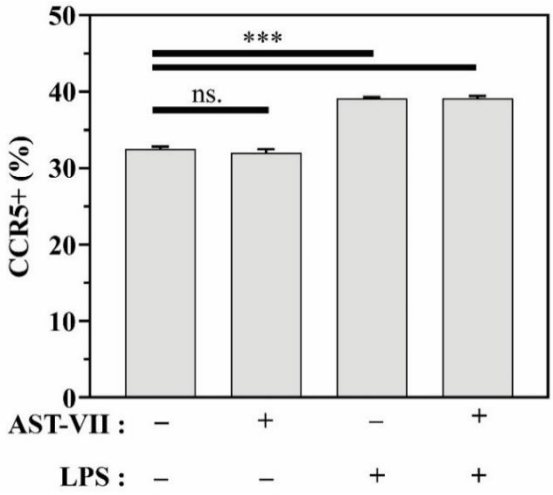

Figure 3.16. CCR5 expression levels on DC2.4 cells treated with AST VII (5 μM), LPS (100 ng/mL), and LPS + AST VII co-treatment. Statistically significant differences in the groups were analyzed using the ordinary one-way ANOVA test. *** $p < 0.001$, ns: non-significant.

Chemotaxis of mDCs is driven by a fine-tuned regulation of chemokine ligands and chemokine receptors where mDCs migrate towards the presence of a chemokine gradient . Therefore, to investigate the CCL5 and CCL2 expression levels in B16-F10

cells, B16-F10 cells were cultured, incubated in RPMI-1640 complete medium, and detached at several time points (12-72 h) to analyze chemokine levels by flow cytometry.

As shown in Figure 3.17A, CCL2 expression in B16-F10 cells decreased over 72 hours. More specifically, the CCL2 expression at 12 hours was 77.2 % and decreased to 59.8 % at the 72-hour time point. Moreover, CCL5 expression levels slightly increased from 64.1 % (12 h) to 71.8 % (72 h) (Figure 3.17B). These data indicated that B16-F10 cells expressed CCR5's corresponding ligands, CCL2 and CCL5.

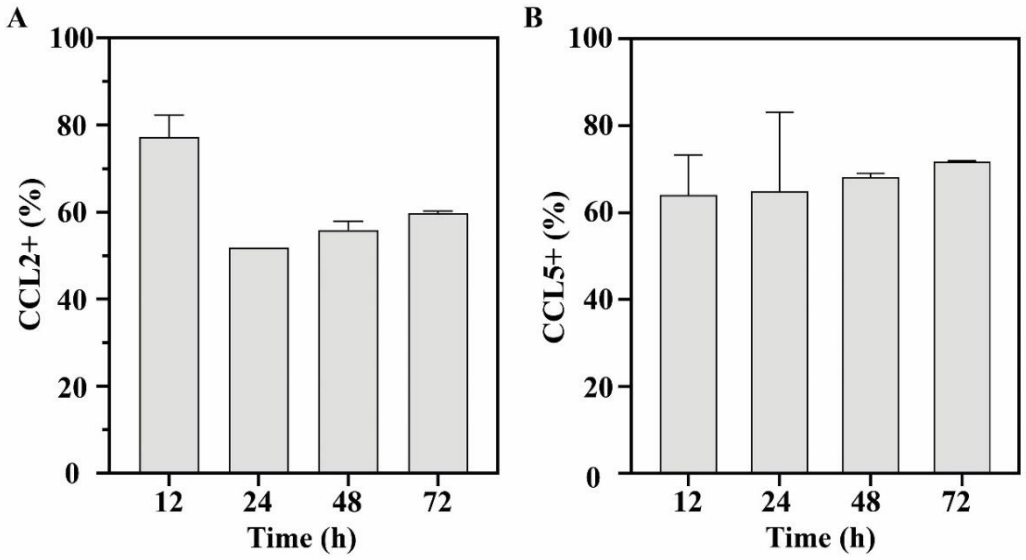

Figure 3.17. Chemokine ligand expression levels in B16-F10 melanoma cells. (A) Chemokine ligand 2 (CCL2) expression levels over a period of 72 hours. (B) Chemokine ligand 5 (CCL5) expression levels over a period of 72 hours.

In light of these data, we expect mDC2.4 cells to undergo chemotaxis towards B16-F10 cells through chemokine gradient, driven dominantly by CCL2 and CCL5 in early and late culture-times, respectively.

3.5. Cytotoxicity Assessment of Small Molecules on Dendritic Cells

The cytotoxicity of LPS and AST-VII on DCs were investigated as relative cell viability. For this purpose, DCs were seeded into the well plate with a starting number of 5-10x 10^3 cells/well and incubated overnight. Then, DCs were treated with (i) only LPS at the concentration of 100 ng/mL, (ii-iii) only AST-VII at 2 and 5 μM concentrations, (iv) LPS (100 ng/mL) and AST-VII (2 μM), and (v) LPS (100 ng/mL) and AST-VII (5 μM) for 24 hours. At the end of treatment, an MTT assay was performed to determine the relative cell viability of DCs.

The DCs ($5x10^3$ cell/well) showed higher cell viabilities compared to the control group (non-treated) for each treatment group at 24 hours (Figure 3.18A). We observed that DCs treated with AST-VII (2-5 μM) had a higher proliferation rate, increasing cell viability. However, lower relative cell viabilities were achieved when the seeding density of DCs was increased to 10^4 cells/well. As shown in Figure 3.18B, the lowest relative cell viability, around 75%, was observed in the group of LPS-only. However, both co-treatment groups (LPS+AST-VII) showed a higher relative cell viability around 84.1% and 90.5 %, respectively. Especially for higher seeding numbers, the co-treatment of DCs with LPS and AST-VII may positively regulate the growth of DCs.

In conclusion, MTT assay results showed no cytotoxic effects of LPS and AST-VII on DCs. As co-treatment of DCs with LPS and AST-VII significantly increased CCR5 expression (Figure 3.16), it also showed higher cell viability.

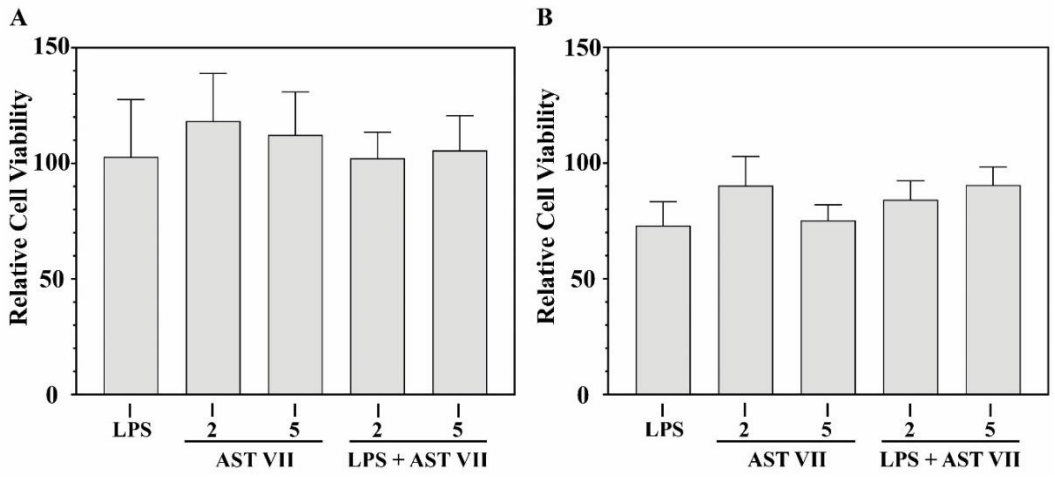

Figure 3.18. Relative cell viability of DCs treated with (i) only LPS (100 ng/mL); (ii-iii) only AST-VII (2-5 μM); (iv) LPS and AST-VII (2 μM); and (v) LPS and AST-VII (5 μM) for seeding cell number of (A) $5x10^3$ cell/well and (B) 10^4 cell/well. The bars represent the average of three experiments, and the error bars indicate the standard deviation.

3.6. Chemotaxis of DCs towards B16-F10 Melanoma Cells in CMDs

The CMDs were previously fabricated and validated for investigating the chemotaxis of DCs towards B16-F10 cells. For this purpose, fluorescence labelled-DCs and B16-F10 cells were co-cultured within CMDs. To confirm chemokine dependent migration of DCs, we performed three different experiments, including (i) treated-DCs (mDCs) vs. None (absence of B16-F10 cells; absence of chemokine), (ii) non-treated-DCs (imDCs) vs B16-F10 cells, and (iii) mDCs vs B16-F10 cells (Figure 3.19).

In the first experimental conditions, mDCs were cultured within the top channel while the bottom channel was empty. As expected, mDCs did not migrate to the bottom channel in the absence of B16-F10 cells and any CCL2/CCL5 chemokine gradient (Figure 3.19A). These findings showed that the developed CMD did not allow mDCs to migrate randomly between top and bottom channels. Additionally, we investigated the migration of imDCs within the CMDs where B16-F10 cells were cultured in the bottom channel as the negative control experimental condition. As shown in Figure 3.19B, imDCs could not cross microchannels to interact with B16-F10 cells over 12 hours. However, a low amount

of fluorescently labelled green mDCs were visualized at the 24-hour time point, in agreement of the lower CCR5 receptor expression in imDCs.

Lastly, we co-cultured mDCs with B16-F10 cells within the top and bottom channels in the CMDs, respectively (Figure 3.19C). While mDCs stayed in their channel at the end of 12 hours, we observed the mDCs by visualizing the green fluorescence in the channel where B16-F10 cells were cultured at 24 hours. However, the red fluorescence showing B16-F10 cells significantly decreased at 24 hours. This observation could be due to possible leaks, contaminations within the CMDs in this experimental condition.

Therefore, as shown in Figure 3.19C, we possibly observed the migratory behavior of LPS+AST-VII co-treated DCs towards B16-F10 cells for 24 hours. In order to overcome these limitations, these experiments will be repeated in triplicates to understand the true chemotaxis ability of mDCs towards B16-F10 cells.

While comparing these three independent experimental conditions, we could possibly indicate that the chemotaxis of DCs was observed through the CCR5/CCL2-CCL5 axis however, to be sure about these results these experiments will be reproduced as future perspectives of this study. According to the obtained results, it can be visualized that chemokine presence is crucial for the directional migration of mDCs towards tumors; this relates with previous reports[149] that have emphasized the importance of chemokine presence for the migration of mDCs towards tumors. Also, higher migrating cells can be observed with maturated DCs compared to imDCs.

At this point, we can possibly conclude that (i) the presence of chemokine ligands and (ii) the maturation of DCs are required and necessary for chemotaxis. These findings also support the literature information about the migratory behavior of mDCs against tumor cells[147,149] or chemokine gradients[120,121,147,149].

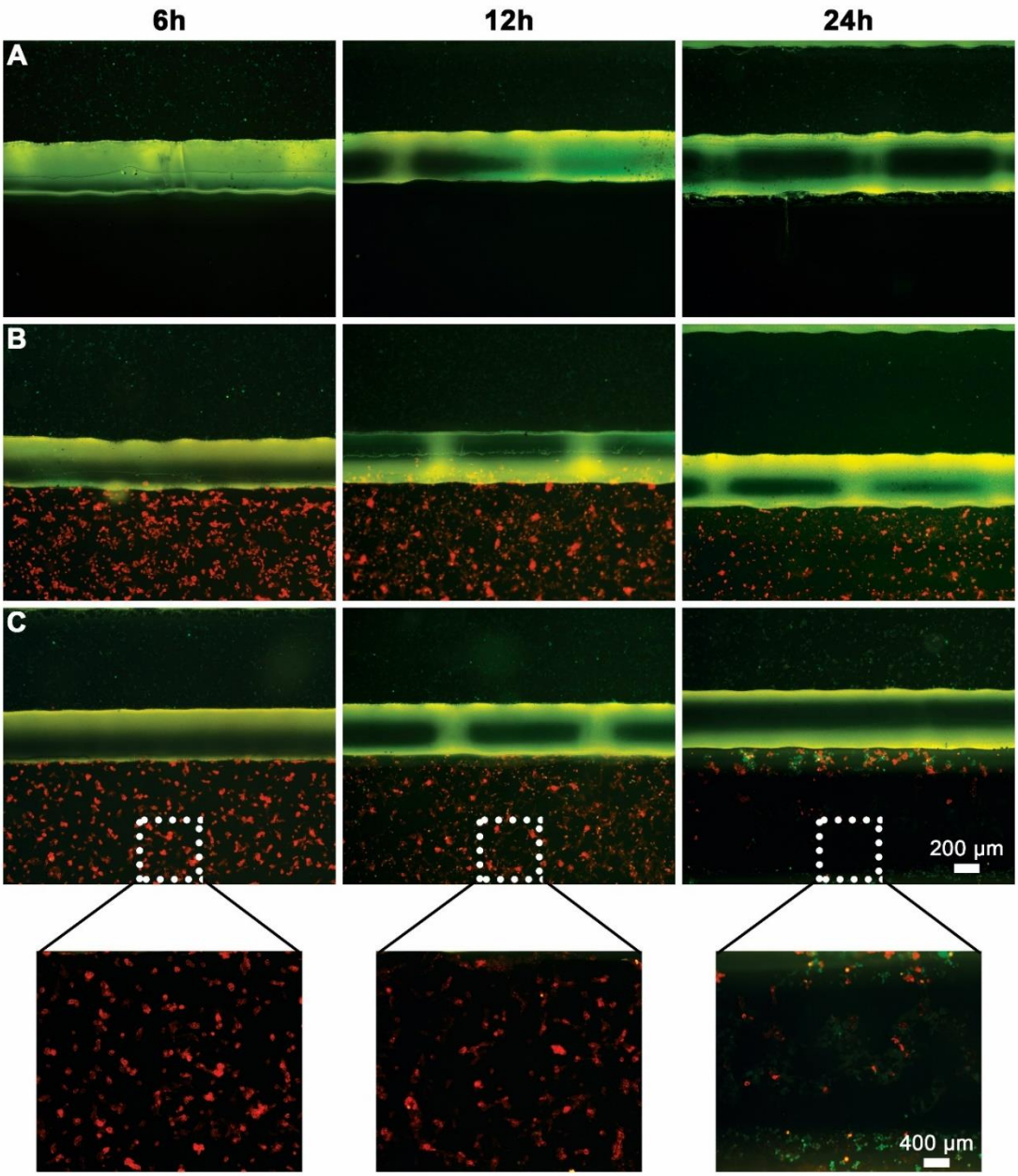

Figure 3.19. Chemotaxis assay. (A) Migration of treated-DCs towards to bottom channel, containing no B16-F10 cells, (B) Migration of untreated-DCs towards B16-F10 cells, (C) Chemotaxis of treated DCs towards B16-F10 cells for 24 hours. Green: DCs, Red: B16-F10 cells.

CHAPTER 4

CONCLUSION

Microfluidic devices have gained significant attention in the last decade due to its numerous advantages, such as high throughput and real-time analysis processing with small amounts of reagent volumes. Recently, microfluidics has been integrated into studying the immune system due to its ability to recapitulate the immune-cancer microenvironment. In this thesis, a chemotaxis microfluidic device (CMD) was designed, developed, and utilized to investigate the chemotaxis of dendritic cells toward melanoma tumors.

In the first section of this thesis, CMD was designed and fabricated through the laser ablation methodology. The fabricated CMDs were then characterized in terms of their structural and mechanical properties, such as microchannel dimensions, properties, liquid handling capacity, and tensile strength. The CMD was designed using AutoCAD and fabricated as a three-layered device having a (i) top layer for inlets and outlets, (ii) middle layer for the top and bottom lateral channels to culture DCs and B16-F10 cells, respectively, and centrally located microchannels, and (iii) bottom layer for support. A laser cutter was used in vector and raster operation modes to fabricate each layer of CMDs. For each operation mode, power (P) (%) and speed (S) (mm s^{-1}) parameters were optimized to pattern desired microchannel patterns onto PMMA. While P80S20 provided the lowest error rate for vector mode, P20S20 offered the required structural properties of microchannels in CMDs. Also, the effects of P and S values on microchannels' width and depth properties were determined for raster mode. Notably, the width and depth values of microchannels increased when the power was increased at a constant speed. After each layer of CMD was obtained, the thermally-assisted solvent bonding technique was utilized using either ethanol or isopropyl alcohol to bond each layer together permanently. The bonding efficacy of CMD layers was evaluated through leakage and tensile tests. The CMD permanently bonded using 80% ethanol at 70°C for 20 minutes and exhibited no leakage and the highest bonding strength. The required amount of liquid sample for the top and bottom channels in CMD was also determined as 60 and 66 μL, respectively.

In the second section of this thesis, the suitability of CMD for cell culture studies was evaluated. The fabricated CMDs were sterilized using either autoclaving or UV light. Then, the viabilities of DC2.4 dendritic (DCs) and B16-F10 melanoma (B16-F10) cells individually cultured in sterilized CMDs were determined using Live/Dead assay. The CMDs sterilized using autoclaving offered higher cell viability of DCs and B16-F10 cells for 48 hours.

In the third section of this thesis, DCs were maturated by stimulating them with small molecules. As we previously reported the maturation of DCs using LPS and AST-VII[159], DCs were stimulated by LPS (100 ng/mL) and AST-VII (2-5 μM). The effects of LPS and AST-VII on the viability of DCs were then investigated. While DCs treatment with LPS-only showed around 75% cell viability, especially for higher cell density, the co-treatment of DCs with LPS and AST-VII provided higher cell viability for low and high cell density. On the other hand, the induction of CCR5 expression in mDCs was determined. It was realized that DCs were synergistically treated with LPS (100 ng/mL), and AST-VII (5 μM) showed higher CCR5 expression. To confirm the chemotaxis of maturated DCs (mDCs) in CMDs depending on the CCR5/CCL2-CCL5 axis, CCL2 and CCL5 expressions in B16-F10 cells were also determined.

In the last section of this thesis, we respectively co-cultured mDCs and B16-F10 cells within the top and bottom channels of CMDs to visualize the time-dependent chemotaxis of mDCs towards B16-F10 cells through the CCR5/CCL2-CCL5 axis. Three experimental conditions were evaluated for the chemotaxis of mDCs. We partially showed the migration of mDCs in the presence of B16-F10 cells towards the CCR5/CCL2-CCL5 axis, while they did not migrate for the condition of the absence of B16-F10 cells and partial migration at 24 hours with treated DCs. We possibly visualized the chemotaxis of DCs co-stimulated with LPS (100 ng/mL) and AST-VII (5 μM) towards B16-F10 cells. However, a significant loss of B16-F10 cells was observed at the 24-hour visualization. This could be due to possible leaks in the bottom lateral channel that could not be visualized by the naked eye, or due to possible contaminations in that specific experimental condition at the 24-hour time point. In order to obtain an accurate understanding of the chemotaxis of DCs treated with LPS-AST-VII, this final experiment is to be performed again to conclude the chemotaxis ability of mDCs towards B16-F10. In these experiments, the study will be performed in triplicates and images will be captured from different locations of the CMDs.

In summary, a PMMA-based three-layered chemotaxis microfluidic device (CMD) was designed via AutoCAD, fabricated through laser ablation, and then used to co-culture DCs and B16-F10 cells. Moreover, the chemotaxis of mDCs towards B16-F10 cells was partially observed in CMDs. The developed microfluidic platform provides a cost-effective, easy-to-fabricate, and time-efficient platform to perform real-time investigations of intercellular interactions.

Future projections with this current work can include the real-time migration of dendritic cells, where migration analysis can be done in terms of their migratory paths and migration velocity. This developed microfluidic platform can be utilized to observe the chemotaxis of mDCs in a dynamic environment cultured with perfusion. Moreover, this PMMA microfluidic platform showed great potential for cell culture applications in terms of cell viability; therefore, PMMA microfluidic devices can be designed and developed for other cell culture applications.

REFERENCES

(1) Mcdonald, J. C.; Duffy, D. C.; Anderson, J. R.; Chiu, D. T.; Wu, H.; Schueller, O. J. A.; Whitesides, G. M. Fabrication of Microfluidic Systems in Poly(Dimethylsiloxane). https://doi.org/10.1002/(SICI)1522-2683(20000101)21:1.

(2) Whitesides, G. M. The Origins and the Future of Microfluidics. *Nature 2006 442:7101* **2006**, *442* (7101), 368–373. https://doi.org/10.1038/nature05058.

(3) Ha, N. S.; De Raad, M.; Han, L. Z.; Golini, A.; Petzold, C. J.; Northen, T. R. Faster, Better, and Cheaper: Harnessing Microfluidics and Mass Spectrometry for Biotechnology. *RSC Chem Biol* **2021**, *2* (5), 1331–1351. https://doi.org/10.1039/D1CB00112D.

(4) Gervais, L.; de Rooij, N.; Delamarche, E. Microfluidic Chips for Point-of-Care Immunodiagnostics. *Advanced Materials* **2011**, *23* (24). https://doi.org/10.1002/adma.201100464.

(5) Terry, S. C.; Jerman, J. H.; Angell, J. B. A Gas Chromatographic Air Analyzer Fabricated on a Silicon Wafer. *IEEE Trans Electron Devices* **1979**, *26* (12), 1880–1886. https://doi.org/10.1109/T-ED.1979.19791.

(6) Convery, N.; Gadegaard, N. 30 Years of Microfluidics. *Micro and Nano Engineering* **2019**, *2*, 76–91. https://doi.org/10.1016/j.mne.2019.01.003.

(7) Ohnstein, T.; Fukiura, T.; Ridley, J.; Bonne, U. Micromachined Silicon Microvalve. In *IEEE Proceedings on Micro Electro Mechanical Systems, An Investigation of Micro Structures, Sensors, Actuators, Machines and Robots.*; IEEE; pp 95–98. https://doi.org/10.1109/MEMSYS.1990.110256.

(8) van Lintel, H. T. G.; van De Pol, F. C. M.; Bouwstra, S. A Piezoelectric Micropump Based on Micromachining of Silicon. *Sensors and Actuators* **1988**, *15* (2), 153–167. https://doi.org/10.1016/0250-6874(88)87005-7.

(9) Reyes, D. R.; Iossifidis, D.; Auroux, P.-A.; Manz, A. Micro Total Analysis Systems. 1. Introduction, Theory, and Technology. *Anal Chem* **2002**, *74* (12), 2623–2636. https://doi.org/10.1021/ac0202435.

(10) Manz, A.; Graber, N.; Widmer, H. M. Miniaturized Total Chemical Analysis Systems: A Novel Concept for Chemical Sensing. *Sens Actuators B Chem* **1990**, *1* (1–6), 244–248. https://doi.org/10.1016/0925-4005(90)80209-I.

(11) Whitesides, G. M.; Ostuni, E.; Takayama, S.; Jiang, X.; Ingber, D. E. Soft Lithography in Biology and Biochemistry. *Annu Rev Biomed Eng* **2001**, *3* (1), 335–373. https://doi.org/10.1146/annurev.bioeng.3.1.335.

(12) Miranda, I.; Souza, A.; Sousa, P.; Ribeiro, J.; Castanheira, E. M. S.; Lima, R.; Minas, G. Properties and Applications of PDMS for Biomedical Engineering: A Review. *J Funct Biomater* **2021**, *13* (1), 2. https://doi.org/10.3390/jfb13010002.

(13) Duffy, D. C.; McDonald, J. C.; Schueller, O. J. A.; Whitesides, G. M. Rapid Prototyping of Microfluidic Systems in Poly(Dimethylsiloxane). *Anal Chem* **1998**, *70* (23), 4974–4984. https://doi.org/10.1021/ac980656z.

(14) Viravaidya, K.; Shuler, M. L. Incorporation of 3T3-L1 Cells To Mimic Bioaccumulation in a Microscale Cell Culture Analog Device for Toxicity Studies. *Biotechnol Prog* **2004**, *20* (2), 590–597. https://doi.org/10.1021/bp034238d.

(15) Martinez, A. W.; Phillips, S. T.; Butte, M. J.; Whitesides, G. M. Patterned Paper as a Platform for Inexpensive, Low-Volume, Portable Bioassays. *Angewandte Chemie International Edition* **2007**, *46* (8), 1318–1320. https://doi.org/10.1002/anie.200603817.

(16) Yeo, L. Y.; Chang, H.; Chan, P. P. Y.; Friend, J. R. Microfluidic Devices for Bioapplications. *Small* **2011**, *7* (1), 12–48. https://doi.org/10.1002/smll.201000946.

(17) Liu, J.; Chen, C.-F.; Tsao, C.-W.; Chang, C.-C.; Chu, C.-C.; DeVoe, D. L. Polymer Microchips Integrating Solid-Phase Extraction and High-Performance Liquid Chromatography Using Reversed-Phase Polymethacrylate Monoliths. *Anal Chem* **2009**, *81* (7), 2545–2554. https://doi.org/10.1021/ac802359e.

(18) Cao, Q.; Mahalanabis, M.; Chang, J.; Carey, B.; Hsieh, C.; Stanley, A.; Odell, C. A.; Mitchell, P.; Feldman, J.; Pollock, N. R.; Klapperich, C. M. Microfluidic Chip for Molecular Amplification of Influenza A RNA in Human Respiratory Specimens. *PLoS One* **2012**, *7* (3), e33176. https://doi.org/10.1371/journal.pone.0033176.

(19) Young, E. W. K.; Beebe, D. J. Fundamentals of Microfluidic Cell Culture in Controlled Microenvironments. *Chem Soc Rev* **2010**, *39* (3), 1036. https://doi.org/10.1039/b909900j.

(20) Huh, D.; Matthews, B. D.; Mammoto, A.; Montoya-Zavala, M.; Hsin, H. Y.; Ingber, D. E. Reconstituting Organ-Level Lung Functions on a Chip. *Science (1979)* **2010**, *328* (5986), 1662–1668. https://doi.org/10.1126/science.1188302.

(21) Jeong, S.-Y.; Lee, J.-H.; Shin, Y.; Chung, S.; Kuh, H.-J. Co-Culture of Tumor Spheroids and Fibroblasts in a Collagen Matrix-Incorporated Microfluidic Chip Mimics Reciprocal Activation in Solid Tumor Microenvironment. *PLoS One* **2016**, *11* (7), e0159013. https://doi.org/10.1371/journal.pone.0159013.

(22) Nielsen, J. B.; Hanson, R. L.; Almughamsi, H. M.; Pang, C.; Fish, T. R.; Woolley, A. T. Microfluidics: Innovations in Materials and Their Fabrication and Functionalization. *Anal Chem* **2020**, *92* (1), 150–168. https://doi.org/10.1021/acs.analchem.9b04986.

(23) Akbari Kenari, M.; Rezvani Ghomi, E.; Akbari Kenari, A.; Arabi, S. M. S.; Deylami, J.; Ramakrishna, S. Biomedical Applications of Microfluidic Devices: Achievements and Challenges. *Polym Adv Technol* **2022**, *33* (12), 3920–3934. https://doi.org/10.1002/pat.5847.

(24) Ren, K.; Zhou, J.; Wu, H. Materials for Microfluidic Chip Fabrication. *Acc Chem Res* **2013**, *46* (11), 2396–2406. https://doi.org/10.1021/ar300314s.

(25) Grover, W. H.; Ivester, R. H. C.; Jensen, E. C.; Mathies, R. A. Development and Multiplexed Control of Latching Pneumatic Valves Using Microfluidic Logical Structures. *Lab Chip* **2006**, *6* (5), 623. https://doi.org/10.1039/b518362f.

(26) Grover, W. H.; Skelley, A. M.; Liu, C. N.; Lagally, E. T.; Mathies, R. A. Monolithic Membrane Valves and Diaphragm Pumps for Practical Large-Scale Integration into Glass Microfluidic Devices. *Sens Actuators B Chem* **2003**, *89* (3), 315–323. https://doi.org/10.1016/S0925-4005(02)00468-9.

(27) Hwang, J.; Cho, Y. H.; Park, M. S.; Kim, B. H. Microchannel Fabrication on Glass Materials for Microfluidic Devices. *International Journal of Precision Engineering and Manufacturing* **2019**, *20* (3), 479–495. https://doi.org/10.1007/s12541-019-00103-2.

(28) Shakeri, A.; Khan, S.; Didar, T. F. Conventional and Emerging Strategies for the Fabrication and Functionalization of PDMS-Based Microfluidic Devices. *Lab Chip* **2021**, *21* (16), 3053–3075. https://doi.org/10.1039/D1LC00288K.

(29) Niculescu, A.-G.; Chircov, C.; Bîrcă, A. C.; Grumezescu, A. M. Fabrication and Applications of Microfluidic Devices: A Review. *Int J Mol Sci* **2021**, *22* (4), 2011. https://doi.org/10.3390/ijms22042011.

(30) Sales, F.; Souza, A.; Ariati, R.; Noronha, V.; Giovanetti, E.; Lima, R.; Ribeiro, J. Composite Material of PDMS with Interchangeable Transmittance: Study of Optical, Mechanical Properties and Wettability. *Journal of Composites Science* **2021**, *5* (4), 110. https://doi.org/10.3390/jcs5040110.

(31) Sia, S. K.; Whitesides, G. M. Microfluidic Devices Fabricated in Poly(Dimethylsiloxane) for Biological Studies. *Electrophoresis* **2003**, *24* (21), 3563–3576. https://doi.org/10.1002/elps.200305584.

(32) Oyama, T. G.; Oyama, K.; Taguchi, M. A Simple Method for Production of Hydrophilic, Rigid, and Sterilized Multi-Layer 3D Integrated Polydimethylsiloxane Microfluidic Chips. *Lab Chip* **2020**, *20* (13), 2354–2363. https://doi.org/10.1039/D0LC00316F.

(33) Damiati, L. A.; El-Yaagoubi, M.; Damiati, S. A.; Kodzius, R.; Sefat, F.; Damiati, S. Role of Polymers in Microfluidic Devices. *Polymers (Basel)* **2022**, *14* (23), 5132. https://doi.org/10.3390/polym14235132.

(34) Tsao, C.-W. Polymer Microfluidics: Simple, Low-Cost Fabrication Process Bridging Academic Lab Research to Commercialized Production. *Micromachines (Basel)* **2016**, *7* (12), 225. https://doi.org/10.3390/mi7120225.

(35) Liu, K.; Fan, Z. H. Thermoplastic Microfluidic Devices and Their Applications in Protein and DNA Analysis. *Analyst* **2011**, *136* (7), 1288. https://doi.org/10.1039/c0an00969e.

(36) van Midwoud, P. M.; Janse, A.; Merema, M. T.; Groothuis, G. M. M.; Verpoorte, E. Comparison of Biocompatibility and Adsorption Properties of Different

Plastics for Advanced Microfluidic Cell and Tissue Culture Models. *Anal Chem* **2012**, *84* (9), 3938–3944. https://doi.org/10.1021/ac300771z.

(37) Persson, H.; Park, S.; Mohan, M.; Cheung, K. K.; Simmons, C. A.; Young, E. W. K. Rapid Assembly of PMMA Microfluidic Devices with PETE Membranes for Studying the Endothelium. *Sens Actuators B Chem* **2022**, *356*, 131342. https://doi.org/10.1016/j.snb.2021.131342.

(38) Mortelmans, T.; Kazazis, D.; Padeste, C.; Berger, P.; Li, X.; Ekinci, Y. Poly(Methyl Methacrylate)-Based Nanofluidic Device for Rapid and Multiplexed Serological Antibody Detection of SARS-CoV-2. *ACS Appl Nano Mater* **2022**, *5* (1), 517–526. https://doi.org/10.1021/acsanm.1c03309.

(39) Niculescu, A.-G.; Chircov, C.; Bîrcă, A. C.; Grumezescu, A. M. Fabrication and Applications of Microfluidic Devices: A Review. *Int J Mol Sci* **2021**, *22* (4), 2011. https://doi.org/10.3390/ijms22042011.

(40) Pupinyo, N.; Chatatikun, M.; Chiabchalard, A.; Laiwattanapaisal, W. *In Situ* Paper-Based 3D Cell Culture for Rapid Screening of the Anti-Melanogenic Activity. *Analyst* **2019**, *144* (1), 290–298. https://doi.org/10.1039/C8AN01725E.

(41) Ozefe, F.; Arslan Yildiz, A. Fabrication and Development of a Microfluidic Paper-Based Immunosorbent Assay Platform (MPISA) for Colorimetric Detection of Hepatitis C. *Analyst* **2023**, *148* (4), 898–905. https://doi.org/10.1039/D2AN01761J.

(42) Campbell, S. B.; Wu, Q.; Yazbeck, J.; Liu, C.; Okhovatian, S.; Radisic, M. Beyond Polydimethylsiloxane: Alternative Materials for Fabrication of Organ-on-a-Chip Devices and Microphysiological Systems. *ACS Biomater Sci Eng* **2021**, *7* (7), 2880–2899. https://doi.org/10.1021/acsbiomaterials.0c00640.

(43) Mantha, S.; Pillai, S.; Khayambashi, P.; Upadhyay, A.; Zhang, Y.; Tao, O.; Pham, H. M.; Tran, S. D. Smart Hydrogels in Tissue Engineering and Regenerative Medicine. *Materials* **2019**, *12* (20), 3323. https://doi.org/10.3390/ma12203323.

(44) Fallahi, H.; Zhang, J.; Phan, H.-P.; Nguyen, N.-T. Flexible Microfluidics: Fundamentals, Recent Developments, and Applications. *Micromachines (Basel)* **2019**, *10* (12), 830. https://doi.org/10.3390/mi10120830.

(45) Alrifaiy, A.; Lindahl, O. A.; Ramser, K. Polymer-Based Microfluidic Devices for Pharmacy, Biology and Tissue Engineering. *Polymers (Basel)* **2012**, *4* (3), 1349–1398. https://doi.org/10.3390/polym4031349.

(46) Tsao, C.-W. Polymer Microfluidics: Simple, Low-Cost Fabrication Process Bridging Academic Lab Research to Commercialized Production. *Micromachines (Basel)* **2016**, *7* (12), 225. https://doi.org/10.3390/mi7120225.

(47) Halldorsson, S.; Lucumi, E.; Gómez-Sjöberg, R.; Fleming, R. M. T. Advantages and Challenges of Microfluidic Cell Culture in Polydimethylsiloxane Devices. *Biosens Bioelectron* **2015**, *63*, 218–231. https://doi.org/10.1016/j.bios.2014.07.029.

(48) Regehr, K. J.; Domenech, M.; Koepsel, J. T.; Carver, K. C.; Ellison-Zelski, S. J.; Murphy, W. L.; Schuler, L. A.; Alarid, E. T.; Beebe, D. J. Biological Implications of Polydimethylsiloxane-Based Microfluidic Cell Culture. *Lab Chip* **2009**, *9* (15), 2132. https://doi.org/10.1039/b903043c.

(49) Giri, K.; Tsao, C.-W. Recent Advances in Thermoplastic Microfluidic Bonding. *Micromachines (Basel)* **2022**, *13* (3), 486. https://doi.org/10.3390/mi13030486.

(50) Ma, X.; Li, R.; Jin, Z.; Fan, Y.; Zhou, X.; Zhang, Y. Injection Molding and Characterization of PMMA-Based Microfluidic Devices. *Microsystem Technologies* **2020**, *26* (4), 1317–1324. https://doi.org/10.1007/s00542-019-04662-2.

(51) Niculescu, A.-G.; Chircov, C.; Bîrcă, A. C.; Grumezescu, A. M. Fabrication and Applications of Microfluidic Devices: A Review. *Int J Mol Sci* **2021**, *22* (4), 2011. https://doi.org/10.3390/ijms22042011.

(52) Bhujbal, S. V.; Dekov, M.; Ottesen, V.; Dunker, K.; Lale, R.; Sletmoen, M. Effect of Design Geometry, Exposure Energy, Cytophilic Molecules, Cell Type and Load in Fabrication of Single-Cell Arrays Using Micro-Contact Printing. *Sci Rep* **2020**, *10* (1), 15213. https://doi.org/10.1038/s41598-020-72080-w.

(53) Dkhar, D. S.; Kumari, R.; Malode, S. J.; Shetti, N. P.; Chandra, P. Integrated Lab-on-a-Chip Devices: Fabrication Methodologies, Transduction System for Sensing Purposes. *J Pharm Biomed Anal* **2023**, *223*, 115120. https://doi.org/10.1016/j.jpba.2022.115120.

(54) Reynolds, D. E.; Lewallen, O.; Galanis, G.; Ko, J. A Customizable and Low-Cost Ultraviolet Exposure System for Photolithography. *Micromachines (Basel)* **2022**, *13* (12), 2129. https://doi.org/10.3390/mi13122129.

(55) Lakshminarayanan, S. Micro/Nano Patterning on Polymers Using Soft Lithography Technique. In *Micro/Nanolithography - A Heuristic Aspect on the Enduring Technology*; InTech, 2018. https://doi.org/10.5772/intechopen.72885.

(56) Xia, Y.; Whitesides, G. M. SOFT LITHOGRAPHY. *Annual Review of Materials Science* **1998**, *28* (1), 153–184. https://doi.org/10.1146/annurev.matsci.28.1.153.

(57) Deshmukh, S. S.; Goswami, A. Recent Developments in Hot Embossing – a Review. *Materials and Manufacturing Processes* **2021**, *36* (5), 501–543. https://doi.org/10.1080/10426914.2020.1832691.

(58) Chien, R.-D. Hot Embossing of Microfluidic Platform. *International Communications in Heat and Mass Transfer* **2006**, *33* (5), 645–653. https://doi.org/10.1016/j.icheatmasstransfer.2006.01.017.

(59) Shakeri, A.; Khan, S.; Jarad, N. A.; Didar, T. F. The Fabrication and Bonding of Thermoplastic Microfluidics: A Review. *Materials* **2022**, *15* (18), 6478. https://doi.org/10.3390/ma15186478.

(60) Piotter, V.; Hanemann, T.; Ruprecht, R.; Haußelt, J. Injection Molding and Related Techniques for Fabrication of Microstructures. *Microsystem Technologies* **1997**, *3* (3), 129–133. https://doi.org/10.1007/s005420050069.

(61) Attia, U. M.; Marson, S.; Alcock, J. R. Micro-Injection Moulding of Polymer Microfluidic Devices. *Microfluid Nanofluidics* **2009**, *7* (1), 1–28. https://doi.org/10.1007/s10404-009-0421-x.

(62) *Polymer Science and Engineering*; National Academies Press: Washington, D.C., 1994. https://doi.org/10.17226/2307.

(63) Agrawal, A. R.; Pandelidis, I. O.; Pecht, M. Injection-Molding Process Control?A Review. *Polym Eng Sci* **1987**, *27* (18), 1345–1357. https://doi.org/10.1002/pen.760271802.

(64) Prabhakar, P.; Sen, R. K.; Dwivedi, N.; Khan, R.; Solanki, P. R.; Srivastava, A. K.; Dhand, C. 3D-Printed Microfluidics and Potential Biomedical Applications. *Frontiers in Nanotechnology* **2021**, *3*. https://doi.org/10.3389/fnano.2021.609355.

(65) Damiati, L. A.; El-Yaagoubi, M.; Damiati, S. A.; Kodzius, R.; Sefat, F.; Damiati, S. Role of Polymers in Microfluidic Devices. *Polymers (Basel)* **2022**, *14* (23), 5132. https://doi.org/10.3390/polym14235132.

(66) Scott, S.; Ali, Z. Fabrication Methods for Microfluidic Devices: An Overview. *Micromachines (Basel)* **2021**, *12* (3), 319. https://doi.org/10.3390/mi12030319.

(67) Chen, C.; Mehl, B. T.; Munshi, A. S.; Townsend, A. D.; Spence, D. M.; Martin, R. S. 3D-Printed Microfluidic Devices: Fabrication, Advantages and Limitations—a Mini Review. *Analytical Methods* **2016**, *8* (31), 6005–6012. https://doi.org/10.1039/C6AY01671E.

(68) Ravi-Kumar, S.; Lies, B.; Zhang, X.; Lyu, H.; Qin, H. Laser Ablation of Polymers: A Review. *Polym Int* **2019**, *68* (8), 1391–1401. https://doi.org/10.1002/pi.5834.

(69) Roberts, M. A.; Rossier, J. S.; Bercier, P.; Girault, H. UV Laser Machined Polymer Substrates for the Development of Microdiagnostic Systems. *Anal Chem* **1997**, *69* (11), 2035–2042. https://doi.org/10.1021/ac961038q.

(70) Klank, H.; Kutter, J. P.; Geschke, O. CO2-Laser Micromachining and Back-End Processing for Rapid Production of PMMA-Based Microfluidic Systems. *Lab Chip* **2002**, *2* (4), 242. https://doi.org/10.1039/b206409j.

(71) Prakash, S.; Kumar, S. Determining the Suitable CO2 Laser Based Technique for Microchannel Fabrication on PMMA. *Opt Laser Technol* **2021**, *139*, 107017. https://doi.org/10.1016/j.optlastec.2021.107017.

(72) Han, X.; Zhang, Y.; Tian, J.; Wu, T.; Li, Z.; Xing, F.; Fu, S. Polymer-based Microfluidic Devices: A Comprehensive Review on Preparation and Applications. *Polym Eng Sci* **2022**, *62* (1), 3–24. https://doi.org/10.1002/pen.25831.

(73) Mirgissa, K. A.; Lee, W.; Kim, D. Toward Rapid Prototyping of High-Aspect-Ratio Sub-$\mathbf{100}-\mu \mathbf{m}$ PMMA Microfluidic Devices: Optimization of CO_2 Laser Machining and Solvent-Assisted Thermal Bonding. In *2019 IEEE 32nd International Conference on Micro Electro Mechanical*

Systems (MEMS); IEEE, 2019; pp 384–386. https://doi.org/10.1109/MEMSYS.2019.8870861.

(74) Ren, Y.; Ray, S.; Liu, Y. Reconfigurable Acrylic-Tape Hybrid Microfluidics. *Sci Rep* **2019**, *9* (1), 4824. https://doi.org/10.1038/s41598-019-41208-y.

(75) Wang, X.; Liedert, C.; Liedert, R.; Papautsky, I. A Disposable, Roll-to-Roll Hot-Embossed Inertial Microfluidic Device for Size-Based Sorting of Microbeads and Cells. *Lab Chip* **2016**, *16* (10), 1821–1830. https://doi.org/10.1039/C6LC00215C.

(76) Young, E. W. K.; Berthier, E.; Guckenberger, D. J.; Sackmann, E.; Lamers, C.; Meyvantsson, I.; Huttenlocher, A.; Beebe, D. J. Rapid Prototyping of Arrayed Microfluidic Systems in Polystyrene for Cell-Based Assays. *Anal Chem* **2011**, *83* (4), 1408–1417. https://doi.org/10.1021/ac102897h.

(77) Novak, R.; Ranu, N.; Mathies, R. A. Rapid Fabrication of Nickel Molds for Prototyping Embossed Plastic Microfluidic Devices. *Lab Chip* **2013**, *13* (8), 1468. https://doi.org/10.1039/c3lc41362d.

(78) Lee, U. N.; Su, X.; Guckenberger, D. J.; Dostie, A. M.; Zhang, T.; Berthier, E.; Theberge, A. B. Fundamentals of Rapid Injection Molding for Microfluidic Cell-Based Assays. *Lab Chip* **2018**, *18* (3), 496–504. https://doi.org/10.1039/C7LC01052D.

(79) Kim, Y.; Song, J.; Lee, Y.; Cho, S.; Kim, S.; Lee, S.-R.; Park, S.; Shin, Y.; Jeon, N. L. High-Throughput Injection Molded Microfluidic Device for Single-Cell Analysis of Spatiotemporal Dynamics. *Lab Chip* **2021**, *21* (16), 3150–3158. https://doi.org/10.1039/D0LC01245A.

(80) Lounsbury, J. A.; Karlsson, A.; Miranian, D. C.; Cronk, S. M.; Nelson, D. A.; Li, J.; Haverstick, D. M.; Kinnon, P.; Saul, D. J.; Landers, J. P. From Sample to PCR Product in under 45 Minutes: A Polymeric Integrated Microdevice for Clinical and Forensic DNA Analysis. *Lab Chip* **2013**, *13* (7), 1384. https://doi.org/10.1039/c3lc41326h.

(81) Matellan, C.; del Río Hernández, A. E. Cost-Effective Rapid Prototyping and Assembly of Poly(Methyl Methacrylate) Microfluidic Devices. *Sci Rep* **2018**, *8* (1), 6971. https://doi.org/10.1038/s41598-018-25202-4.

(82) Murphy, K. (Kenneth M.); Weaver, C.; Janeway, C. *Janeway's Immunobiology*.

(83) Delves, P. J.; Roitt, I. M. The Immune System. *New England Journal of Medicine* **2000**, *343* (1), 37–49. https://doi.org/10.1056/NEJM200007063430107.

(84) Kupper, T. S.; Fuhlbrigge, R. C. Immune Surveillance in the Skin: Mechanisms and Clinical Consequences. *Nat Rev Immunol* **2004**, *4* (3), 211–222. https://doi.org/10.1038/nri1310.

(85) Gasteiger, G.; Rudensky, A. Y. Interactions between Innate and Adaptive Lymphocytes. *Nat Rev Immunol* **2014**, *14* (9), 631–639. https://doi.org/10.1038/nri3726.

(86) Koenderman, L.; Buurman, W.; Daha, M. R. The Innate Immune Response. *Immunol Lett* **2014**, *162* (2), 95–102. https://doi.org/10.1016/j.imlet.2014.10.010.

(87) Marshall, J. S.; Warrington, R.; Watson, W.; Kim, H. L. An Introduction to Immunology and Immunopathology. *Allergy, Asthma & Clinical Immunology* **2018**, *14* (S2), 49. https://doi.org/10.1186/s13223-018-0278-1.

(88) *From Innate Immunity to Immunological Memory*; Pulendran, B., Ahmed, R., Eds.; Springer Berlin Heidelberg: Berlin, Heidelberg, 2006; Vol. 311. https://doi.org/10.1007/3-540-32636-7.

(89) Banchereau, J.; Briere, F.; Caux, C.; Davoust, J.; Lebecque, S.; Liu, Y.-J.; Pulendran, B.; Palucka, K. Immunobiology of Dendritic Cells. *Annu Rev Immunol* **2000**, *18* (1), 767–811. https://doi.org/10.1146/annurev.immunol.18.1.767.

(90) Banchereau, J.; Steinman, R. M. Dendritic Cells and the Control of Immunity. *Nature* **1998**, *392* (6673), 245–252. https://doi.org/10.1038/32588.

(91) Thomas, R.; Lipsky, P. E. Dendritic Cells: Origin and Differentiation. *Stem Cells* **1996**, *14* (2), 196–206. https://doi.org/10.1002/stem.140196.

(92) Martin-Gayo, E.; Yu, X. G. Role of Dendritic Cells in Natural Immune Control of HIV-1 Infection. *Front Immunol* **2019**, *10*. https://doi.org/10.3389/fimmu.2019.01306.

(93) Kim, R.; Emi, M.; Tanabe, K. Functional Roles of Immature Dendritic Cells in Impaired Immunity of Solid Tumour and Their Targeted Strategies for Provoking Tumour Immunity. *Clin Exp Immunol* **2006**, *146* (2), 189–196. https://doi.org/10.1111/j.1365-2249.2006.03215.x.

(94) Andreae, S.; Piras, F.; Burdin, N.; Triebel, F. Maturation and Activation of Dendritic Cells Induced by Lymphocyte Activation Gene-3 (CD223). *The Journal of Immunology* **2002**, *168* (8), 3874–3880. https://doi.org/10.4049/jimmunol.168.8.3874.

(95) Soto, J. A.; Gálvez, N. M. S.; Andrade, C. A.; Pacheco, G. A.; Bohmwald, K.; Berrios, R. V.; Bueno, S. M.; Kalergis, A. M. The Role of Dendritic Cells During Infections Caused by Highly Prevalent Viruses. *Front Immunol* **2020**, *11*. https://doi.org/10.3389/fimmu.2020.01513.

(96) Dixon, G. L. J.; Newton, P. J.; Chain, B. M.; Katz, D.; Andersen, S. R.; Wong, S.; van der Ley, P.; Klein, N.; Callard, R. E. Dendritic Cell Activation and Cytokine Production Induced by Group B *Neisseria Meningitidis* : Interleukin-12 Production Depends on Lipopolysaccharide Expression in Intact Bacteria. *Infect Immun* **2001**, *69* (7), 4351–4357. https://doi.org/10.1128/IAI.69.7.4351-4357.2001.

(97) Oth, T.; Vanderlocht, J.; Van Elssen, C. H. M. J.; Bos, G. M. J.; Germeraad, W. T. V. Pathogen-Associated Molecular Patterns Induced Crosstalk between Dendritic Cells, T Helper Cells, and Natural Killer Helper Cells Can Improve

Dendritic Cell Vaccination. *Mediators Inflamm* **2016**, *2016*, 1–12. https://doi.org/10.1155/2016/5740373.

(98) Askew, D.; Chu, R. S.; Krieg, A. M.; Harding, C. V. CpG DNA Induces Maturation of Dendritic Cells with Distinct Effects on Nascent and Recycling MHC-II Antigen-Processing Mechanisms. *The Journal of Immunology* **2000**, *165* (12), 6889–6895. https://doi.org/10.4049/jimmunol.165.12.6889.

(99) Reis e Sousa, C. Dendritic Cells in a Mature Age. *Nat Rev Immunol* **2006**, *6* (6), 476–483. https://doi.org/10.1038/nri1845.

(100) Kim, M. K.; Kim, J. Properties of Immature and Mature Dendritic Cells: Phenotype, Morphology, Phagocytosis, and Migration. *RSC Adv* **2019**, *9* (20), 11230–11238. https://doi.org/10.1039/C9RA00818G.

(101) Tai, Y.; Wang, Q.; Korner, H.; Zhang, L.; Wei, W. Molecular Mechanisms of T Cells Activation by Dendritic Cells in Autoimmune Diseases. *Front Pharmacol* **2018**, *9*. https://doi.org/10.3389/fphar.2018.00642.

(102) Tiberio, L.; Del Prete, A.; Schioppa, T.; Sozio, F.; Bosisio, D.; Sozzani, S. Chemokine and Chemotactic Signals in Dendritic Cell Migration. *Cell Mol Immunol* **2018**, *15* (4), 346–352. https://doi.org/10.1038/s41423-018-0005-3.

(103) Randolph, G. J.; Angeli, V.; Swartz, M. A. Dendritic-Cell Trafficking to Lymph Nodes through Lymphatic Vessels. *Nat Rev Immunol* **2005**, *5* (8), 617–628. https://doi.org/10.1038/nri1670.

(104) Jin, T.; Xu, X.; Hereld, D. Chemotaxis, Chemokine Receptors and Human Disease. *Cytokine* **2008**, *44* (1), 1–8. https://doi.org/10.1016/j.cyto.2008.06.017.

(105) Liu, J.; Zhang, X.; Cheng, Y.; Cao, X. Dendritic Cell Migration in Inflammation and Immunity. *Cell Mol Immunol* **2021**, *18* (11), 2461–2471. https://doi.org/10.1038/s41423-021-00726-4.

(106) Nagarsheth, N.; Wicha, M. S.; Zou, W. Chemokines in the Cancer Microenvironment and Their Relevance in Cancer Immunotherapy. *Nat Rev Immunol* **2017**, *17* (9), 559–572. https://doi.org/10.1038/nri.2017.49.

(107) Bachelerie, F.; Graham, G. J.; Locati, M.; Mantovani, A.; Murphy, P. M.; Nibbs, R.; Rot, A.; Sozzani, S.; Thelen, M. An Atypical Addition to the Chemokine Receptor Nomenclature: <scp>IUPHAR</Scp> Review 15. *Br J Pharmacol* **2015**, *172* (16), 3945–3949. https://doi.org/10.1111/bph.13182.

(108) Johnson, L. A.; Jackson, D. G. Inflammation-Induced Secretion of CCL21 in Lymphatic Endothelium Is a Key Regulator of Integrin-Mediated Dendritic Cell Transmigration. *Int Immunol* **2010**, *22* (10), 839–849. https://doi.org/10.1093/intimm/dxq435.

(109) de Winde, C. M.; Munday, C.; Acton, S. E. Molecular Mechanisms of Dendritic Cell Migration in Immunity and Cancer. *Med Microbiol Immunol* **2020**, *209* (4), 515–529. https://doi.org/10.1007/s00430-020-00680-4.

(110) Liu, Y.; Shi, G. Role of G Protein-Coupled Receptors in Control of Dendritic Cell Migration. *Biomed Res Int* **2014**, *2014*, 1–11. https://doi.org/10.1155/2014/738253.

(111) Foti, M.; Granucci, F.; Aggujaro, D.; Liboi, E.; Luini, W.; Minardi, S.; Mantovani, A.; Sozzani, S.; Ricciardi-Castagnoli, P. Upon Dendritic Cell (DC) Activation Chemokines and Chemokine Receptor Expression Are Rapidly Regulated for Recruitment and Maintenance of DC at the Inflammatory Site. *Int Immunol* **1999**, *11* (6), 979–986. https://doi.org/10.1093/intimm/11.6.979.

(112) Zhao, X.; Sato, A.; Dela Cruz, C. S.; Linehan, M.; Luegering, A.; Kucharzik, T.; Shirakawa, A.-K.; Marquez, G.; Farber, J. M.; Williams, I.; Iwasaki, A. CCL9 Is Secreted by the Follicle-Associated Epithelium and Recruits Dome Region Peyer's Patch CD11b+ Dendritic Cells. *The Journal of Immunology* **2003**, *171* (6), 2797–2803. https://doi.org/10.4049/jimmunol.171.6.2797.

(113) Vecchi, A.; Massimiliano, L.; Ramponi, S.; Luini, W.; Bernasconi, S.; Bonecchi, R.; Allavena, P.; Parmentier, M.; Mantovani, A.; Sozzani, S. Differential Responsiveness to Constitutive vs. Inducible Chemokines of Immature and Mature Mouse Dendritic Cells. *J Leukoc Biol* **1999**, *66* (3), 489–494. https://doi.org/10.1002/jlb.66.3.489.

(114) Jimenez, F.; Quinones, M. P.; Martinez, H. G.; Estrada, C. A.; Clark, K.; Garavito, E.; Ibarra, J.; Melby, P. C.; Ahuja, S. S. CCR2 Plays a Critical Role in Dendritic Cell Maturation: Possible Role of CCL2 and NF-KB. *The Journal of Immunology* **2010**, *184* (10), 5571–5581. https://doi.org/10.4049/jimmunol.0803494.

(115) Robays, L. J.; Maes, T.; Lebecque, S.; Lira, S. A.; Kuziel, W. A.; Brusselle, G. G.; Joos, G. F.; Vermaelen, K. V. Chemokine Receptor CCR2 but Not CCR5 or CCR6 Mediates the Increase in Pulmonary Dendritic Cells during Allergic Airway Inflammation. *The Journal of Immunology* **2007**, *178* (8), 5305–5311. https://doi.org/10.4049/jimmunol.178.8.5305.

(116) Oppermann, M. Chemokine Receptor CCR5: Insights into Structure, Function, and Regulation. *Cell Signal* **2004**, *16* (11), 1201–1210. https://doi.org/10.1016/j.cellsig.2004.04.007.

(117) Payne, A. S.; Cornelius, L. A. The Role of Chemokines in Melanoma Tumor Growth and Metastasis. *Journal of Investigative Dermatology* **2002**, *118* (6), 915–922. https://doi.org/10.1046/j.1523-1747.2002.01725.x.

(118) Kadomoto, S.; Izumi, K.; Mizokami, A. Roles of CCL2-CCR2 Axis in the Tumor Microenvironment. *Int J Mol Sci* **2021**, *22* (16), 8530. https://doi.org/10.3390/ijms22168530.

(119) Dieu, M.-C.; Vanbervliet, B.; Vicari, A.; Bridon, J.-M.; Oldham, E.; Aït-Yahia, S.; Brière, F.; Zlotnik, A.; Lebecque, S.; Caux, C. Selective Recruitment of Immature and Mature Dendritic Cells by Distinct Chemokines Expressed in Different Anatomic Sites. *J Exp Med* **1998**, *188* (2), 373–386. https://doi.org/10.1084/jem.188.2.373.

(120) Haessler, U.; Kalinin, Y.; Swartz, M. A.; Wu, M. An Agarose-Based Microfluidic Platform with a Gradient Buffer for 3D Chemotaxis Studies. *Biomed Microdevices* **2009**, *11* (4), 827–835. https://doi.org/10.1007/s10544-009-9299-3.

(121) Ricart, B. G.; John, B.; Lee, D.; Hunter, C. A.; Hammer, D. A. Dendritic Cells Distinguish Individual Chemokine Signals through CCR7 and CXCR4. *The Journal of Immunology* **2011**, *186* (1), 53–61. https://doi.org/10.4049/jimmunol.1002358.

(122) Wendland, M.; Czeloth, N.; Mach, N.; Malissen, B.; Kremmer, E.; Pabst, O.; Förster, R. CCR9 Is a Homing Receptor for Plasmacytoid Dendritic Cells to the Small Intestine. *Proceedings of the National Academy of Sciences* **2007**, *104* (15), 6347–6352. https://doi.org/10.1073/pnas.0609180104.

(123) Pierce, C. W.; Solliday, S. M.; Asofsky, R. IMMUNE RESPONSES IN VITRO. *J Exp Med* **1972**, *135* (3), 675–697. https://doi.org/10.1084/jem.135.3.675.

(124) Gordon, S. Elie Metchnikoff: Father of Natural Immunity. *Eur J Immunol* **2008**, *38* (12), 3257–3264. https://doi.org/10.1002/eji.200838855.

(125) Shanti, A.; Teo, J.; Stefanini, C. In Vitro Immune Organs-on-Chip for Drug Development: A Review. *Pharmaceutics* **2018**, *10* (4), 278. https://doi.org/10.3390/pharmaceutics10040278.

(126) Brehm, M. A.; Bortell, R.; Verma, M.; Shultz, L. D.; Greiner, D. L. Humanized Mice in Translational Immunology. In *Translational Immunology*; Elsevier, 2016; pp 285–326. https://doi.org/10.1016/B978-0-12-801577-3.00012-5.

(127) Sinha, N.; Subedi, N.; Tel, J. Integrating Immunology and Microfluidics for Single Immune Cell Analysis. *Front Immunol* **2018**, *9*. https://doi.org/10.3389/fimmu.2018.02373.

(128) Cheng, X.; Irimia, D.; Dixon, M.; Sekine, K.; Demirci, U.; Zamir, L.; Tompkins, R. G.; Rodriguez, W.; Toner, M. A Microfluidic Device for Practical Label-Free CD4+ T Cell Counting of HIV-Infected Subjects. *Lab Chip* **2007**, *7* (2), 170–178. https://doi.org/10.1039/B612966H.

(129) Li, P.; Gao, Y.; Pappas, D. Multiparameter Cell Affinity Chromatography: Separation and Analysis in a Single Microfluidic Channel. *Anal Chem* **2012**, *84* (19), 8140–8148. https://doi.org/10.1021/ac302002a.

(130) Qiu, L.; Wimmers, F.; Weiden, J.; Heus, H. A.; Tel, J.; Figdor, C. G. A Membrane-Anchored Aptamer Sensor for Probing IFNγ Secretion by Single Cells. *Chemical Communications* **2017**, *53* (57), 8066–8069. https://doi.org/10.1039/C7CC03576D.

(131) Ahn, J.; Barber, G. N. STING Signaling and Host Defense against Microbial Infection. *Exp Mol Med* **2019**, *51* (12), 1–10. https://doi.org/10.1038/s12276-019-0333-0.

(132) Kawasaki, T.; Kawai, T. Toll-Like Receptor Signaling Pathways. *Front Immunol* **2014**, *5*. https://doi.org/10.3389/fimmu.2014.00461.

(133) Liu, T.; Zhang, L.; Joo, D.; Sun, S.-C. NF-KB Signaling in Inflammation. *Signal Transduct Target Ther* **2017**, *2* (1), 17023. https://doi.org/10.1038/sigtrans.2017.23.

(134) Campisi, M.; Sundararaman, S. K.; Shelton, S. E.; Knelson, E. H.; Mahadevan, N. R.; Yoshida, R.; Tani, T.; Ivanova, E.; Cañadas, I.; Osaki, T.; Lee, S. W. L.; Thai, T.; Han, S.; Piel, B. P.; Gilhooley, S.; Paweletz, C. P.; Chiono, V.; Kamm, R. D.; Kitajima, S.; Barbie, D. A. Tumor-Derived CGAMP Regulates Activation of the Vasculature. *Front Immunol* **2020**, *11*. https://doi.org/10.3389/fimmu.2020.02090.

(135) Tay, S.; Hughey, J. J.; Lee, T. K.; Lipniacki, T.; Quake, S. R.; Covert, M. W. Single-Cell NF-KB Dynamics Reveal Digital Activation and Analogue Information Processing. *Nature* **2010**, *466* (7303), 267–271. https://doi.org/10.1038/nature09145.

(136) Vesperini, D.; Montalvo, G.; Qu, B.; Lautenschläger, F. Characterization of Immune Cell Migration Using Microfabrication. *Biophys Rev* **2021**, *13* (2), 185–202. https://doi.org/10.1007/s12551-021-00787-9.

(137) Junkin, M.; Tay, S. Microfluidic Single-Cell Analysis for Systems Immunology. *Lab Chip* **2014**, *14* (7), 1246. https://doi.org/10.1039/c3lc51182k.

(138) Businaro, L.; De Ninno, A.; Schiavoni, G.; Lucarini, V.; Ciasca, G.; Gerardino, A.; Belardelli, F.; Gabriele, L.; Mattei, F. Cross Talk between Cancer and Immune Cells: Exploring Complex Dynamics in a Microfluidic Environment. *Lab Chip* **2013**, *13* (2), 229–239. https://doi.org/10.1039/C2LC40887B.

(139) Hampton, H. R.; Chtanova, T. Lymphatic Migration of Immune Cells. *Front Immunol* **2019**, *10*. https://doi.org/10.3389/fimmu.2019.01168.

(140) Sokol, C. L.; Luster, A. D. The Chemokine System in Innate Immunity. *Cold Spring Harb Perspect Biol* **2015**, *7* (5), a016303. https://doi.org/10.1101/cshperspect.a016303.

(141) Schwarz, J.; Bierbaum, V.; Merrin, J.; Frank, T.; Hauschild, R.; Bollenbach, T.; Tay, S.; Sixt, M.; Mehling, M. A Microfluidic Device for Measuring Cell Migration towards Substrate-Bound and Soluble Chemokine Gradients. *Sci Rep* **2016**, *6* (1), 36440. https://doi.org/10.1038/srep36440.

(142) Lin, F. Chapter 15 A Microfluidics-Based Method for Analyzing Leukocyte Migration to Chemoattractant Gradients; 2009; pp 333–347. https://doi.org/10.1016/S0076-6879(09)05415-9.

(143) Li Jeon, N.; Baskaran, H.; Dertinger, S. K. W.; Whitesides, G. M.; Van De Water, L.; Toner, M. Neutrophil Chemotaxis in Linear and Complex Gradients of Interleukin-8 Formed in a Microfabricated Device. *Nat Biotechnol* **2002**, *20* (8), 826–830. https://doi.org/10.1038/nbt712.

(144) Lin, F.; Nguyen, C. M.-C.; Wang, S.-J.; Saadi, W.; Gross, S. P.; Jeon, N. L. Effective Neutrophil Chemotaxis Is Strongly Influenced by Mean IL-8

Concentration. *Biochem Biophys Res Commun* **2004**, *319* (2), 576–581. https://doi.org/10.1016/j.bbrc.2004.05.029.

(145) Ren, X.; Getschman, A. E.; Hwang, S.; Volkman, B. F.; Klonisch, T.; Levin, D.; Zhao, M.; Santos, S.; Liu, S.; Cheng, J.; Lin, F. Investigations on T Cell Transmigration in a Human Skin-on-Chip (SoC) Model. *Lab Chip* **2021**, *21* (8), 1527–1539. https://doi.org/10.1039/D0LC01194K.

(146) Parlato, S.; Grisanti, G.; Sinibaldi, G.; Peruzzi, G.; Casciola, C. M.; Gabriele, L. Tumor-on-a-Chip Platforms to Study Cancer–Immune System Crosstalk in the Era of Immunotherapy. *Lab Chip* **2021**, *21* (2), 234–253. https://doi.org/10.1039/D0LC00799D.

(147) Hwang, H.; Shin, C.; Park, J.; Kang, E.; Choi, B.; Han, J.-A.; Do, Y.; Ryu, S.; Cho, Y.-K. Human Breast Cancer-Derived Soluble Factors Facilitate CCL19-Induced Chemotaxis of Human Dendritic Cells. *Sci Rep* **2016**, *6* (1), 30207. https://doi.org/10.1038/srep30207.

(148) Aizel, K.; Clark, A. G.; Simon, A.; Geraldo, S.; Funfak, A.; Vargas, P.; Bibette, J.; Vignjevic, D. M.; Bremond, N. A Tuneable Microfluidic System for Long Duration Chemotaxis Experiments in a 3D Collagen Matrix. *Lab Chip* **2017**, *17* (22), 3851–3861. https://doi.org/10.1039/C7LC00649G.

(149) Parlato, S.; De Ninno, A.; Molfetta, R.; Toschi, E.; Salerno, D.; Mencattini, A.; Romagnoli, G.; Fragale, A.; Roccazzello, L.; Buoncervello, M.; Canini, I.; Bentivegna, E.; Falchi, M.; Bertani, F. R.; Gerardino, A.; Martinelli, E.; Natale, C.; Paolini, R.; Businaro, L.; Gabriele, L. 3D Microfluidic Model for Evaluating Immunotherapy Efficacy by Tracking Dendritic Cell Behaviour toward Tumor Cells. *Sci Rep* **2017**, *7* (1), 1093. https://doi.org/10.1038/s41598-017-01013-x.

(150) Atalis, A.; Dixon, J. B.; Roy, K. Soluble and Microparticle-Based Delivery of TLR4 and TLR9 Agonists Differentially Modulate 3D Chemotaxis of Bone Marrow-Derived Dendritic Cells (Adv. Healthcare Mater. 15/2021). *Adv Healthc Mater* **2021**, *10* (15). https://doi.org/10.1002/adhm.202170068.

(151) Abcam. *Cell Tracking Dye Kit - Red - Cytopainter (ab138893)*. https://www.abcam.com/ps/products/138/ab138893/documents/cell-tracking-dye-kit-protocol-book-v2c-ab138893%20(website).pdf.

(152) Abcam. *Cell Tracking Dye Kit - Green - Cytopainter (ab138891)*. https://www.abcam.com/ps/products/138/ab138891/documents/ab138891%20CytoPainter%20Cell%20Tracking%20Staining%20Kit%20-%20Green%20Fluorescence%20v3a%20(website).pdf.

(153) Rodriguez-Moncayo, R.; Gonzalez-Suarez, A. M.; López-Ortega, O.; Garcia-Cordero, J. L. Microfluidic Tools to Study Cell Migration. In *Cell Movement in Health and Disease*; Elsevier, 2022; pp 273–293. https://doi.org/10.1016/B978-0-323-90195-6.00016-4.

(154) Davidson, P. M.; Sliz, J.; Isermann, P.; Denais, C.; Lammerding, J. Design of a Microfluidic Device to Quantify Dynamic Intra-Nuclear Deformation during Cell

Migration through Confining Environments. *Integrative Biology* **2015**, *7* (12), 1534–1546. https://doi.org/10.1039/C5IB00200A.

(155) Bamshad, A.; Nikfarjam, A.; Khaleghi, H. A New Simple and Fast Thermally-Solvent Assisted Method to Bond PMMA–PMMA in Micro-Fluidics Devices. *Journal of Micromechanics and Microengineering* **2016**, *26* (6), 065017. https://doi.org/10.1088/0960-1317/26/6/065017.

(156) Kohli, K.; Pillarisetty, V. G.; Kim, T. S. Key Chemokines Direct Migration of Immune Cells in Solid Tumors. *Cancer Gene Ther* **2022**, *29* (1), 10–21. https://doi.org/10.1038/s41417-021-00303-x.

(157) Vilgelm, A. E.; Richmond, A. Chemokines Modulate Immune Surveillance in Tumorigenesis, Metastasis, and Response to Immunotherapy. *Front Immunol* **2019**, *10*. https://doi.org/10.3389/fimmu.2019.00333.

(158) Messina, J. L.; Fenstermacher, D. A.; Eschrich, S.; Qu, X.; Berglund, A. E.; Lloyd, M. C.; Schell, M. J.; Sondak, V. K.; Weber, J. S.; Mulé, J. J. 12-Chemokine Gene Signature Identifies Lymph Node-like Structures in Melanoma: Potential for Patient Selection for Immunotherapy? *Sci Rep* **2012**, *2* (1), 765. https://doi.org/10.1038/srep00765.

(159) Yakubogullari, N.; Cagir, A.; Bedir, E.; Sag, D. Astragalus Saponins, Astragaloside VII and Newly Synthesized Derivatives, Induce Dendritic Cell Maturation and T Cell Activation. *Vaccines (Basel)* **2023**, *11* (3), 495. https://doi.org/10.3390/vaccines11030495.